Growth of fiberform nanostructures on metal surfaces by helium plasma irradiation

Shin Kajita,[1, a] Atsushi M. Ito,[2, 3] and Kenzo Ibano[4]

[1] *Graduate School of Frontier Sciences, the University of Tokyo, 5-1-5 Kashiwanoha, Kashiwa, Chiba 277-8561, Japan*

[2] *National Institute for Fusion Science, Natural Institutes of Natural Sciences, 322-6 Oroshi-cho, Toki, 509-5292, Japan*

[3] *The Graduate University for Advanced Studies (SOKENDAI), 322-6 Oroshi-cho, Toki, 509-5292, Japan*

[4] *Graduate School of Engineering, Osaka University, Suita, Osaka 565-0871, Japan*

(Dated: 13 October 2022)

Helium plasma irradiation to various metals leads to peculiar morphology changes as forming fiberform nanostructures called *fuzz* when a certain set of conditions is satisfied. In this Tutorial, we overview experimental observations about the fuzz growth process, conditions, growth rate etc. on tungsten (W), and fuzz growth observed on other various metals. The fuzz growth mechanism, open questions about fuzz growth, and current understandings on these issues are discussed based on simulation and theoretical works. Several applications (gas sensors and photocatalytic application) with fuzz are shown. We hope that this Tutorial will help new researchers in this field to perform experiments and simulations to reveal new perspectives of fuzz.

---

[a] Electronic mail: kajita@k.u-tokyo.ac.jp

I. INTRODUCTION

Since helium (He) atoms are one of the byproducts of nuclear fusion reaction (nuclear fusion between deuterium and tritium), interaction between He ions and materials, tungsten (W) in particular, has been investigated experimentally, because W is the most plausible candidate material for divertor in fusion devices, where the heat load is concentrated. Initially, investigations had been done using high energy ion beams. Formation of high density He bubbles has been identified on W after the irradiation with 8 keV He^+ ions[1] even when the He ion fluence, Φ_{He}, was less than 10^{21} m^{-2}. This could be understandable because the energy was greater than the threshold energy of He for the displacement of W atoms. Later it was found that He bubble growth can occur even when the incident ion energy, E_i, is much lower than the sputtering threshold, and the necessary energy for the bubble formation is shown to be less than 10 eV[2].

The surprising thing is that when certain conditions for T_s, E_i, and Φ_{He} are satisfied[3,4], fiberform nanostructures are formed, and the surface becomes completely black. It is noted that the conditions are likely to be met under the strike point in the divertor. Figure 1(a,b) shows cross-sectional scanning electron microscope (SEM) micrographs of W fiberform nanostructures. The fiberform nanostructure is called *fuzz*. As shown by a transmission electron microscope (TEM) image in Figure 1(c), the width of the nanostructure is several tens of nm and contains many He bubbles inside the fibers. The size of He bubbles is less than 20-30 nm in diameter, and the size of bubbles and width of fibers are known to increase as increasing the surface temperature[5,6].

It has been revealed that the formation of fuzz changes various physical properties. The porosity of the fuzzy layer was measured by measuring the mass and thickness of the fuzzy layer[7]. The porosity increases with increasing Φ_{He}, and it becomes about 95% when the thickness of the fuzzy layer, h_{fuzz}, is about 3 μm. It was also found that the density of fuzzy layer is not uniform but it gradually decreases in the height direction[8]. The surface area increases by the formation of fuzz and reaches 20-30 times higher than that of a flat surface when h_{fuzz} is several μm[9]. In terms of the interaction of particles (ions and electrons), the sputtering rate decreases by about an order of magnitude[7], particle reflectivity decreases, resulting in an increase in the power transfer coefficient[10]; secondary electron emission (SEE) decreases by about 50% and is reported to be uncorrelated with the direction of electron bombardment[11]. In addition, the field electron emission is found to increase significantly compared to the unirradiated surfaces, and the field enhancement factor is confirmed to increase to ∼1000[12,13]. The work function increases by about 0.5 eV[14]. The thermal conductivity, which determines the interaction with heat, was found to decrease by at least two orders of magnitude from the thermoreflectance method[15]. Other than that, the optical reflectance decreased to almost zero from ultraviolet (UV) to near infrared (NIR) (more than 99%)[16], and the optical emissivity increased as a result[17].

These material property changes raise concerns for the material life time in nuclear fusion reactor, because the erosion processes become complicated by the existence of fuzz. Fuzz growth is a particular concern in fusion devices from a perspective of long-term operation, because it may occur on the divertor for a short period of time, i.e. within less than an hour. Therefore, extensive studies have been performed on W because of the interest in fusion research. On the one hand, there are several positive aspects as plasma facing components in fusion reactors. The decrease in the sputtering yield decreases the erosion by sputtering. In addition, it has also been found that the crack formation due to intermittent heat loading is inhibited by the formation of fuzz[18]. On the other hand, the formation of fuzz can have a significant negative effect on thermal responses. Since the thickness of the nanostructures is only a few micrometers meters at most, the surface temperature does not increase with a steady heat load. However, intermittent heat loads can lead to significant differences between temperature responses with and without the fuzzy layer. Pulsed laser irradiation experiments on fuzz in vacuum (a pulse width of ∼0.5 ms)[19] and on fuzz simultaneously irradiated with pulsed or steady state plasma[20] showed that melting traces on the surface with an excessive surface temperature increase. In addition to an anomalous temperature rise and melting, the frequency of arcing increases when the surface is covered with fuzz[21,22]. An arcing on material that is exposed to plasmas is called unipolar arc, because it occurs between material (cathode) and the plasma, unlike the usual arcing that occurs between a cathode and an anode. When a localized arcing occurs, a large amount of W is emitted, which can cause significant damage to material and may also be a source of impurities in fusion reactors. In particular, since fuzz is extremely fragile mechanically, it can form dusts and droplets as was observed in response to ignition of arcing[23], which is a major concern for the reactor operation.

As mentioned above, fuzz is an important issue in nuclear fusion research. Figure 2(a,b) shows number of fuzz related publications per year and journal, respectively. It is noted that there are relevant papers that are not included in Fig. 2. For example, since the term *fuzz* has not been used commonly before 2010, the number of publications is almost zero, although there are several important relevant papers. However, we can see the trend of the number of fuzz related publications here. The number of relevant published papers began to increase around 2010, with 80-100 papers published annually since 2017. Mainly, the research field is in the nuclear material researches and relevant basic material researches published in such as *J. Nucl. Mater.*, *Nucl. Fusion*, and *Nucl. Mat. Energy.* In addition, since it is expected to be used also for various applications, there are several dozen papers published in applied physics field such as in *J. Appl. Phys.* and *Appl. Surf. Sci.*

In this tutorial, we will focus on fuzz and discuss our understanding to date and the issues that need to be solved in the future. We also present applications of fuzz as gas sensor and photocatalysts. In Sec. II, we firstly show fuzz growth on W, mainly because there are extensive experimental studies on W. Sec. III discusses fuzz on W alloys and various metals, and Sec. IV summarizes modeling and simulation works up to date. Then, open issues and future prospects of fuzz are discussed.

II. FUZZ GROWTH ON W

A. Growth process

TEM micrographs of W samples exposed to He plasmas with different Φ_{He} are shown in Fig. 3(a) (0.6×10^{25} m^{-2}) to Fig. 3(e)(5.5×10^{25} m^{-2})[16]. It is seen that h_{fuzz} increases with Φ_{He}. Initially, rough structures are formed on the surface. The surface top layer (∼100 nm thick) is fully packed with He bubbles (Fig. 3(a)), followed by the formation of protrusions (Fig. 3(b)). Then, fiberform nanostructures are started to be observed from Fig. 3(c). From thermal desorption spectroscopy (TDS), He content in fuzz was estimated to be He/W = $(13\pm4)\%$[24]. It is believed that the formation and growth of He bubbles are the key process for the growth of fuzz. As shown in a schematic of Fig. 4, the growth of bubbles formed protrusions, and swelling process due to the inclusion of He atoms and bubbles with increasing the porosity is likely related to the initial growth process. The details of the growth process will be discussed later in Sec. IV.

B. Formation condition

From experiments in the linear plasma devices NAGDIS-II and PISCES-B, it has been shown that T_s and E_i are important conditions for the fuzz growth. Figure 5 summarizes the growth condition of fuzz in terms of T_s and E_i. The gray colored area and hatched area represent the conditions where fuzz growth and bubble growth are identified, respectively. In Fig. 5, bubbles mean pinholes observed on the surface rather than nanobubbles observed by TEM. The fuzz formation requires T_s of 1000-2000 K and E_i of greater than or equal to 20-30 eV. Another important parameter is Φ_{He}, and Fig. 6 shows the summary of h_{fuzz} versus Φ_{He} organized by Petty *et al.*[25]. It has been shown experimentally that h_{fuzz} is proportional to the square root of Φ_{He}[26], suggesting that some diffusion-like process limits the growth of the fuzz layer. Also, by plotting h_{fuzz} as a function of Φ_{He}, it was revealed that the intersection point with the horizontal is not always zero, indicating existence of an incubation fluence (typically $\Phi_{\mathrm{He},0} = 2.5\times10^{24}$ m^{-2}) that precedes the fuzz growth[27]. It is noted that fuzz growth has been reported not only from high density ($> 10^{18}$ m^{-3}) linear plasma devices, but also from magnetron sputtering devices, where the plasma density is lower[28]. A difference from the higher density devices is in the fact that fuzz was identified even when Φ_{He} is lower than or comparable to the incubation fluence of $\Phi_{\mathrm{He},0} = 2.5\times10^{24}$ m^{-2} in magnetron sputtering devices[29].

C. Crystal orientation

In the initial phase of the morphology changes, i.e., when the fluence or the energy of the incident ions is low, dependence on the crystal orientation of the fuzz growth can be detected, although no clear dependence remains when fuzz is fully grown. Ohno *et al.* investigated the initial morphology changes and crystal orientations by the combination of electron backscatter diffraction (EBSD) and SEM observation[30], as shown in Fig. 7. In Ref. 30, E_i was chosen to be 25 eV, which is close to the threshold energy for the fuzz growth. Clear wavy structures were found on {101} face, while the surface was kept flat on {102}, {407}, and {203} faces with pinholes on the surface. Similar results were reported by Parish *et al.* using SEM-EBSD[31], in which morphology changes on W exposed to a He plasma up to a He fluence of 4×10^{24} m^{-2} at $T_s = 1130$ °C were investigated around {001} plane. They categorized the morphology changes to smooth, pyramidal, wavy and terraced, and revealed the relation between the types of morphology changes and crystal orientation. It was shown that pyramids were formed near-$\langle 001\rangle$||normal direction (ND) grains, wavy/terraced were formed near $\langle 114\rangle$ to $\langle 112\rangle$||ND grains, and the surface remained smooth near $\langle 103\rangle$||ND grains.

The difference between Refs. 30 and 31 appeared on $\{001\}$ plane, where wavy and pyramid structures were observed, respectively. In another report, He irradiation on single crystal W showed that initial morphology changes on $\{001\}$ plane was less than that on $\{101\}$ plane[32]. Near-$\{001\}$ planes, the mophology change was different (flat, pyramidal, and wavy). One clue is in the dependence of crystal orientation on the interval of undulation formed at temperatures below the threshold temperature for fuzz formation studied in detail by Sakamoto *et al.*[33,34]. It was found that the crests of undulation align with the $\langle 100\rangle$ direction. In other words, $\{001\}$ plane can be more stable than the other planes. At the moment, it is not yet clear how these mophology change occur, though slip and adatom diffusion are candidates for this.

Crystal orientation of isolated nano-tendrils from W fuzz has been investigated using transmission Kikuchi diffraction[35]. It was shown that there was no preferential crystal orientation in the long axis (growth direction) for W fuzz. However, preferential growth direction was identified on Re and Ru fuzz[36]. On Re and Ru fuzz, fibers have no bifurcation, and curved wires grew *c*-axis direction in hexagonal closed packed (HCP) crystal structure.

D. Sputtering and annealing

There are processes that counteract the growth of fuzz: sputtering and high-temperature annealing. The sputtering yield decreases by an order of magnitude when fuzz is formed on the surface[7], as mentioned in introduction, probably because the sputtered atoms are trapped again by the fuzzy structure. However, since the growth rate continuously decreases with increasing h_{fuzz}, while sputtering rate does not decrease more than one order of magnitude, the effective growth rate approaches zero. The saturation in fuzz growth can be clearly identified especially when the sputtering effect is significant. The threshold energy for He ions to sputter W atoms is approximately 105-110 eV[37]. The saturation thickness is determined by the balance between the growth rate and the sputtering yield[38] and decreases from $7-8$ μm at 200 eV to less than 1 μm at 400 eV[39]. It could be changed if the prompt redeposition of sputtered particles would occur[40]. It is noted that the sputtering can also occur even when $E_i < 100$ eV. Petty et al. discussed that a small amount of background impurity, which can be usually neglected, cannot be neglected to determine the thickness[25] when Φ_{He} is significantly greater than 10^{27} m^{-2}.

Another process that counteracted fuzz growth is the thermal annealing process. It has been found that fuzz can be reintegrated to surface even at temperatures much lower than the melting point of 3700 K[41–43]. Typically, a 500-nm-thick fuzzy layer was reintegrated to the surface by a 30-min thermal annealing at a temperature of ~1400 K. The annealing rate exponentially increases with the annealing temperature. De Temmerman *et al.* summarized the available experimental data and modeled the annealing rate with double exponential Arrhenius-type functions[44]. It was shown that trends of the temperature dependence of the annealing rate changes around ~1550 K. Even without erosion by sputtering, the thickness saturates by the equilibrium between the growth rate and the annealing rate[45]. In fusion reactor environment, annealing during the transient heat load accompanied by instabilities called edge localized modes (ELMs) can be influential for the saturation fuzzy layer thickness[44].

E. Non-uniform growth

Woller *et al.* discovered that large-scale structures of tens of micrometers in size, called nano tendril bundles (NTBs), can be formed by He irradiation[46]. They discussed that the radio frequency (RF) bias of the target and the broad ion energy are related to the growth process. Furthermore, NTBs were found to form (Fig. 8) when a small amount of impurity, such as argon, neon, and nitrogen, was added to He gas, suggesting that the redeposition of W released by sputtering is important[47]. The role of impurity in the growth of a large-scale structure 10-μm in size has also been discussed with the existence of small amount of carbon (0.01%)[48]. Woller *et al.* made a comparison between EBSD images and SEM and optical micrographs of the samples that has two separate regions where full fuzz growth and NTB growth are dominant, respectively[49]. They showed that NTB growth occurs easier on the surface that has {101} than the surface with other orientations. It was discussed that the results supported surface diffusion or W adatom mobility enhanced by ion bombardment plays a key role in the NTB formation.

It has been revealed that the NTBs significantly decrease the onset electric field of the field electron emission and increase the field electron emission current[50]. Because the field electron emission can lead to the initiation of unipolar arcing[51], understanding of growth process of NTB will be important for fusion experiments.

F. Enhanced growth

In addition, in recent years, it has been found that fuzz grows at orders of magnitude higher rates than the normal growth rate during He irradiation with metal atoms/ions deposition, and visible fuzzy nanostructures with a thickness of about 1 mm are formed after about 30-60 min of irradiation[52]. Figure 9(a,b) shows an optical micrograph and an SEM image of the large-scale fiberform nanostructures (LFNs). It can be seen that fiberform nanostructures with a width of several tens of nm are intertwined to form the large-scale structure. This result suggests that the presence of metal atoms deposited on the surface causes the growth of LFNs via different process and growth rate than conventional fuzz.

Enhanced growth of fuzz with auxiliary W deposition has also been identified in a magnetron sputtering device[53] in addition to linear plasma devices[54,55]. The growth rate does not follow the square root of Φ_{He} anymore with additional deposition. In the magnetron sputtering device, 8-μm-thick fuzz was formed when Φ_{He} was less than 10^{25} m^{-2}. Considering that such thick fuzzy layer can be formed only when Φ_{He} is $\sim 10^{27} - 10^{28}$ m^{-2} in pure He plasmas[25], one can say that additional deposition increases the growth rate by orders of magnitudes. On LFNs shown in Fig. 9(a,b), the structures grew not mainly in height (normal to the surface) direction but in the surface direction (parallel to the surface) after the height reached 0.1 mm, which corresponded to the sheath thickness, and the growth rate in the surface direction was estimated to be $\sim$7 μm/s[56]. It is noted that the growth rate does not saturate nor decrease with Φ_{He}.

Figure 10 summarizes the thickness or height of nanostructures grown in He plasmas. For conventional fuzz, the thickness increases with square root of Φ_{He} and saturates probably because of sputtering. The thickness could not exceed 10 μm even if Φ_{He} was greater than 10^{27} m^{-2}. The height of NTBs is 10-40 μm when Φ_{He} is the order of 10^{25} m^{-2}. With auxiliary deposition, the thickness reached $\sim$7 μm at $\Phi_{\mathrm{He}} \sim 10^{26}$ m^{-2} in Magnum-PSI[54] and 8 μm at $\Phi_{\mathrm{He}} \sim 10^{25}$ m^{-2} in a magnetron sputtering device[53]. When LFN growth occurred, the height reached 200 μm in the initial phase of deposition experiments (LFNs growth) even at Φ_{He} of 10^{25} m^{-2}. The thickness reached 1 mm when Φ_{He} was 4×10^{25} m^{-2}. The growth of LFNs was identified when W/He ratio was greater than 0.04%, and the growth rate could be altered by the ratio of W/He.

In the initial phase of the LFN growth, the height of fibers increases exponentially in time[56]. Thus, one can say that bottom-growth process such as tin whiskers[57], which was formed by in-plane compressive stress, cannot explain the exponential growth. Also, from the crystal orientation analysis of ruthenium and rhenium (Re) fuzz, it was found that the fibers are straight and the growth direction is always *c*-axis direction of hexagonal closed packed (HCP) crystal structure[36]. It is thought that the adatom formed by the deposition of metallic atoms on the fiber surface diffused on the fiber, and epitaxial growth occurs on the tip of the fiber.

Concerning the exponential growth up to 0.1 mm, one potential explanation is the effects of electric field around the fibers. When the height of the fiber is much shorter than the sheath thickness, the trajectories of ions to the surface was not influenced by the fibers. However, when the height is comparable to or greater than the sheath thickness, the electric field formed around the fibers likely attract the metal and He ions[52]. That will accelerate the numbers of adatoms formed on the fiber surface. Although the detailed mechanisms for enhanced fuzz growth with deposition has yet to be fully understood, understanding of the enhanced growth process will shed light on the study of the fuzz growth mechanism.

III. FUZZ GROWTH ON VARIOUS METALS

A. W alloys and mixture layer

Helium plasma irradiations to doped W and W alloys have been performed from an early stage. Baldwin *al.* irradiated He plasmas to doped W grades - La_2O_3 (1wt%), Re (5wt% and 10wt%), and TiC (1.5wt%)[41]. Kajita *et al.* used doped W with undersized atomic species (Fe 2at% and Cr 2at%)[32]. Fuzz was grown on all the doped W samples in the same manner as pure W cases. Concerning Re, quantitative comparison in the growth rate of fuzzy layer showed additional Re has an inhibiting effect on growth[58]. Because transmutation of W to

Re is expected in fusion reactors, it is thought to have a beneficial effect.

Helium plasma irradiation using a thin film deposited on a W substrate has revealed an interesting feature. Doerner *et al.* performed He plasma irradiation using a thin film of an isotope-enriched W (∼92.99% ^{182}W) deposited on the surface of a bulk W sample with the natural abundance of the isotopes[59]. It was revealed that the depth profiles of the atoms in the thin film showed that mixing of W atoms from bulk to the surface occurred. They concluded that the results indicate enhanced mixing of W atoms due to the dynamic behavior of He bubbles. Strong mixture during fuzz growth has also been identified on W film on bulk Mo[60] and ruthenium (Ru) and Re thin film on bulk W[61].

B. Pure metals

After the discovery of fuzz structure on W, similar nano-scale structures were found on other metallic materials[4]. Shapes and scales vary by each material, and useful insight can be obtained from comparisons of their structures[62–65]. As seen in Fig. 11, typical fuzz, fiberform nanostructure with a diameter of 20 - 30 nm and a thickness of few micrometer, can be seen on W, molybdenum (Mo), titanium (Ti)[66], and iron (Fe)[66], and various precious metals[65] with a typical He ion fluence of greater than 10^{25} m^{-2}. A thin fuzzy layer appears on the surface of niobium (Nb) and tantalum (Ta) when the ion fluence was sufficiently high ($\sim 10^{26}$ m^{-2}). Fuzz also forms on Re and Ir and grows faster than W fuzz under similar irradiation conditions[63]. The thickness of the fuzzy layer of rhenium (Re) and iridium (Ir) reaches 10 - 100 micrometer with the He ion fluence of $\sim 2\times10^{25}$ m^{-2}. In addition, the formation of fuzz on zirconium (Zr) and hafnium (Hf) was also observed[67].

Fiber on cone shape appears on silver (Ag) and palladium (Pd). On Ag and Pd surfaces, fiberform nanostructures formed only on a tip of cone shape structures. The nanocone formation by He plasma irradiation has been identified on various materials including beryllium[68], chromium (Cr) [69], titanium, stainless steel[66], and silicon[70]. Nishijima *et al.* performed He irradiation to Cr in several linear devices and concluded that deposition of a small amount of heavier impurities (Mo or Ta) was the seed for preferential sputtering leading to the nanocone formation. Shi *et al.* also concluded that the deposition was inevitable for the formation of silicon nanocones, and actively changed the amount of molybdenum deposition on silicon to control the size and the aspect ratio of nanocones[71]. Concerning the fiber on cone structure, the growth mechanism is not yet clear, but the nanofiber at the tip could be made of impurities. First, the cone shape is formed on surface by sputtering, then impurity species diffuse on surface and agglomerate on the tip of the cone, because the impurity-rich tip is less likely sputtered. Finally, the impurity species on the cone form the fiber.

Some materials are hard to show fiberform nanostructures. Compared to the fiberform nanostructures, the nanostructures of gold (Au) and platinum (Pt)[63] have thicker and straight shapes. We call them as *rod-like* structures. Fiberform nanostructure formed on Ta in the NAGDIS-II device[72]. However, because it requires a high He fluence and the sputtering yield is low, Ta is a suitable material for the specimen masks and materials exposed to plasmas in He plasma irradiation experiments.

So, where does this difference in the tendency to form He induced nanostructures between materials come from? One of the key parameters to control the surface morphology change is T_s. First, let us discuss about the surface temperature. As shown in Figs. 5 and 12(a), there are temperature windows for the fuzzy nanostructure growth. Growth of fuzz occurs when the samples were irradiated with He plasmas in the homologous temperature range of $0.25 < T_H < 0.6$, where T_H is defined as

$$T_H = \frac{T_s}{T_m}. \tag{1}$$

Here, the unit of T_s and T_m should be in K. The homologous temperature is a useful measure to estimate the rate of diffusion-dependent deformation, in other words *creep*. In general, creep deformation occurs at $T_H > 0.6$, and the fuzz formation becomes less likely in that temperature range. This upper boundary indicates that the creep process may perturb the growth of the fiber structure.

For both the upper and lower boundaries, the He behavior in lattice could be related. As was discussed in Sec. II, the formation of He bubbles is required for He-induced growth of nanostructures, and T_H is an important parameter for the growth of He bubbles[73]. For the He bubble formation, numbers of He atoms should be migrated, and agglomerated at one site. In general, temperature is a strong factor in the migration of He atoms/clusters. If the temperature is too low, these He migrations are less likely. As the He bubbles with the appropriate size grow in the surface top layer, surface morphology changes occur.

The elastic modulus of materials such as shear modulus, bulk modulus, and Young's modulus can be another key parameter. The importance of the shear modulus has been discussed in terms of the viscoelastic model[74–76], where viscose flow of W to the tip of the fiber plays a key role for the fuzz growth. Although adatom diffusion has recently become more popular to explain the growth process, the elastic modulus still seems to be an important parameter from an experimental point of view. Figure 12(b) summarizes the He plasma induced morphology changes as a function shear modulus of the materials at $T_H = 0.25 - 0.5$. In this figure, materials can be categorized into three groups in terms of the tendency to the fuzz growth: easily formed, only thin layer, and no fuzz. This categorization shows that the fuzz structure growth is preferrable on materials with higher shear modulus. It should be noted that the temperature dependence of the shear modulus can also be important. The error bars represent the minimum and maximum values of shear modulus at $T_H = 0.25 - 0.5$. The fuzz preferrable materials show larger error bars.

In addition to the above factors, sputtering yield is another important parameter, as was discussed in Ref. 72. For example, concerning aluminum and cupper, where fuzz has yet to be identified, the sputtering yield is $\sim$0.08 when $E_i = 100$ eV. Considering that the sputtering yield of W by He is $\sim$0.015 even at $E_i = 500$ eV, where only a thin fuzzy layer ($\sim$300 nm) could form due to the equilibrium between growth and sputtering[39], the significant sputtering may complicate the fuzz growth or narrow the conditional window.

IV. MODELING AND SIMULATION

There is currently no numerical simulation that can fully reproduce the formation and growth of fuzz. Although a direct comparison between simulations and experiments has been difficult yet, the role of simulation is to investigate physical processes from the theoretical viewpoint that cannot be directly observed in experiments and to clarify the mechanism of fuzz formation. The physical processes under He plasma irradiation are complicated and a representative case of a multi-scale multi-physics processes. Therefore, there are a wide variety of simulation methods to be used[77], and some new methods have been developed for research on fuzz.

Figure 13 shows physical processes at the surface and inside W exposed to a He plasma. We describe the relationship between the physical processes involved in fuzz formation and simulation methods suitable for them. When reading or using simulation methods and results, it is important to first recognize whether the calculation is an atomistic model, a coarse-grained model, or a continuous-field model. Atomic models are not always first-principles models, while coarse-grained models and continuous-field models tend to be empirical models. At that time, it is important to carefully find out what kind of mechanism is assumed as driving forces. Here, typical methods of atomistic simulations used for plasma-material interaction (PMI) are Binary Collision Approximation (BCA), Molecular Dynamics (MD), Density Functional Theory (DFT), and Kinetic Monte-Carlo (KMC). These methods should be used properly according to each process in Fig. 13.

A. Injection Process with Binary Collision Approximation

Helium atoms are irradiated from the plasma with an energy of 10 eV to several keV. The He atoms scatter the atoms composing a target material, while a part of He atoms are reflected back into the plasma region and the other He atoms stay inside. To investigate this incident process of He, BCA has been often used. In BCA, the dynamics of multi-particles is approximated as the iteration of two-body collisions between an incident atom and rest target atoms. The incident atom is called projectile culturally. The projectile gradually loses its kinetic energy due to collisions with many target atoms and eventually stops. When the energy transfer from a projectile to a target atom due to a collision is higher than the threshold energy, E_{rc}, the target atom is regarded to be kicked out. The atom kicked out is called recoil or knock-on atom, and it begins to move according to the same routine as the projectile. As a result, the trajectories of projectiles and recoils are obtained like a cascade scattering. When recoils are ejected from a surface, they are counted as sputtered atoms. This is a better approximation when the kinetic energy of the projectile is high and the scattering cross section is small.

Energy transfer from a projectile to a target atom due to a collision becomes maximum when a head-on collision occurs. From this fact, the condition that target atoms are sputtered out by the plasma irradiation with the incident energy, E_{i}, is given by

$$E_{\mathrm{i}} > E_{\mathrm{rc}} \frac{(m_1 + m_2)^2}{4 m_1 m_2}, \tag{2}$$

where m_1 and m_2 are the masses of the incident atom and the target atom, respectively. The right-hand side of Eq. (2) is called sputtering threshold energy. In the case of fuzz formation, m_1 and m_2 are set to the masses of He and W atoms, respectively. Here, it is necessary to pay attention that the threshold energy $E_{\rm rc}$ to generate a recoil has different names depending on BCA codes, such as the *recoil cutoff energy*, *surface binding energy*, or *displacement energy*. Furthermore, the value set as $E_{\rm rc}$ also depends on codes. For example, in TRIM.SP code[78–80] and ACAT code[81,82], $E_{\rm rc}$ is considered as the binding energy at which the target atom is bound by surrounding atoms in the material, and then, the cohesive energy and the sublimation energy are employed as $E_{\rm rc}$. However, SRIM code often employs a value much larger than the cohesive energy. If the cohesive energy of W (8.9 eV) is employed, the sputtering threshold energy of W by a He ion becomes about 107 eV. In most experiments for fuzz formation, the incident energy of He plasma is lower than the sputtering threshold energy of 107 eV. From this point, it had been considered that the sputtering had little effect on fuzz formation. Let us discuss about sputtering again later.

Apart from sputtering, the incident process is also involved in the penetration depth of He from the surface, which is culturally called *range*. The penetration depth of He corresponds to the initial position of thermal diffusion of He in material. Of particular importance, in metals with lattice structures, He atoms often penetrate deeply by *channeling*. Note, however, that some conventional BCA codes can only handle either amorphous structure or crystalline structure.

There seems to be a misunderstanding that BCA is sometimes called the Monte-Carlo method, which is a general term for methods that use random number for simulations and numerical calculations. The random numbers are used for the following two parts in BCA code. One is to determine the initial positions of projectiles. The other is to generate a target atom for each collision. In the past, the BCA code developed for computers with limited memory cannot retain all the atomic positions of a target material. Therefore, when one collision is over, the collision target atom is deleted from computer memory in order to reduce a total memory usage. At the next step, the next collision target atom is generated using random numbers according to the density of the target material. This is probably one reason why the BCA is sometimes called the Monte Carlo method. The other reason why the BCA is sometimes called the Monte Carlo method is probably because it is confused with the binary collision model[83] in particle-in-cell (PIC) simulation in which the trajectory of each collision is determined by using random numbers. On the other hand, the important point of BCA is that in each collision the trajectories of projectiles and target atoms are solved without random number and are uniquely determined as a function of the kinetic energy of projectiles and an impact parameter. Moreover, on recent computers with a larger memory resource, recent BCA codes such as AC∀T[84,85] retain all atomic positions in a target material, and then any structured material can be treated. Namely, the Monte-Carlo method is only to determine incident positions.

The large memory resources of modern computers also make it easier to simulate complicated surface geometries. Retaining the data of about one billion atoms, it is possible to handle full-scale fuzz-like structures of 100^3 nm^3. BCA for the full-scale fuzz-like structure is useful for investigating the effect of nanoscale fibers and their gaps, rather than simply considering the fuzz layer as a low-density uniform material. Nakamura *et al.*[86] made a semi-elliptical hole on the surface. Klaver *et al.*[87] simulated fuzz by stacking ellipsoids in a network. Similarly, Yang *et al.*[88] simulated a fuzz by stacking cylinders in a network. For instance, sputtering yield becomes lower than that of a flat surface because recoils re-deposit on fibers.

B. Density Functional Theory

After He atoms are implanted to material, a key issue is the formation of He bubbles. Let us choose the calculation method depending on whether we need static property or dynamic property. To investigate the nucleation of He bubbles in material, the binding energy of He atoms, which is the energy gain when a He atom moves from an independent interstitial site to a clustering site, is often used and is estimated according to the electronic state calculation using DFT[89,90]. Here, if the binding energy of He atoms is positive, agglomerated He atoms in W are energetically more stable than independent He atoms at interstitial sites. From Fig. 14, the binding energy of He atoms clustering at an interstitial site increases, while that at a mono-vacancy site decreases. However, both of the binding energies remain positive at 2.0 to 2.5 eV even when the number of He atoms in the cluster is greater than eight. This suggests that the agglomeration of He atoms into a larger He bubble will continue. The mechanism why He atom can agglomerate in W is considered as follows. Noble gas atoms, which have an electronically closed shell structure, receive repulsion from electrons in metal. It is stable for them to self-aggregate and to create a space with a low electron density in the metal[91]. Such evaluation of the binding energy of He atoms by DFT is also useful for metals other than W[62]. From Fig. 14, it is clear that He atoms can agglomerate in various elements (W, Mo, Cr, Ta, Nb, vanadium (V), and Fe), which have a body-centered cubic (BCC) structure. In addition, He agglomeration was also confirmed by using DFT for Ir and Au which have face-centered cubic (FCC) structure[92].

C. Molecular Dynamics

MD simulations are often used to investigate dynamical phenomena such as the deformation processes of W due to He bubbles. One of the successful results of MD is a visual demonstration of loop punching. According to the simulation results[93,94], when the size of a He bubble reaches several nm, W atoms around the He bubble are pushed out. The W atoms are not emitted separately but are collectively shifted in $\langle 111 \rangle$ direction. At this time, the lattice mismatch that appears around the pushed atoms is observed as a dislocation loop. By this emission, the pressure in the He bubble is released.

As a He bubble grows near the surface, dislocation loops are emitted toward the surface. As a result, the surface is lifted. When the pressure inside the He bubble is high, part of the lifted surface bursts, which is called bursting. However, according to MD[95,96], the size of the pinhole created by the bursting is less than 1 nm. Still, almost all He atoms escape through pinholes in a few picoseconds. Therefore, the height of the surface that can be lifted is at most about the size of a He bubble. This is not enough to explain fuzz growth. In addition, the size of pinholes created by the bursting in MD is an order of magnitude smaller than experimental observations.

Here, we note that the steps achieved by a typical MD in recent computer system is up to 10^8 per a day, which corresponds to about 10 ns. Therefore, although MD can treat rapid processes such as the diffusion of He and H atoms in material and the loop-punching due to the stress of a He bubble, slower processes such as the thermal annealing and structure relaxation of W are difficult to simulate with MD. For the same reason, MD also hardly treats the process of bubble connection, in which the motion of W atoms causes a slow change in the shape of He bubbles from a dumbbell-shaped to a larger spherical shape.

Since He bubbles can be generated far deeper than the penetration depth of the injection process, the diffusion of He atoms is important for the distribution of He bubbles. The diffusion process of He atoms in W is involved in the distribution of He bubbles and the generation of surface roughness. According to DFT estimates, the migration barrier energy of He in W with a BCC lattice is ΔE =0.04–0.06 eV[91,97]. This is less than one-third of the migration barrier energy of 0.2 eV for hydrogen atoms. Moreover, the migration barrier energies of Ne and Ar, which are noble gases, are about the same as or less than the migration barrier energy of hydrogen atoms.

It is not possible to estimate the diffusion coefficient just by using the DFT. The diffusion coefficient is given as a function of the temperature by $D(T) = D_0 \exp(-\Delta E/k_\mathrm{b}T)$. We either estimate the pre-factor D_0 of the diffusion coefficient using transition state theory[98,99] or estimate the mean squared displacement observed from an actual diffusion trajectory in MD. For the latter case, D_0 and ΔE are determined by the Arrhenius plot. In fact, the MD simulations reported that $D_0 = 5.35 \times 10^{-8}$ m$^2/s$, $\Delta E = 0.13$ eV[100], and $D_0 = 3.36 \times 10^{-8}$ m$^2/s$, $\Delta E = 0.0623$ eV[101], where these difference was caused by the difference of potential models. The estimations suggested that the diffusion speed of He atoms is faster than that of hydrogen atoms. In addition, it is important that He atoms can diffuse even if they form a cluster such as a dimer and a trimer. Moreover, both MD[100] and DFT showed that the diffusion speed of a dimer is faster than that of a single atom.

D. Flux and Fluence in Simulation

The fact from experiments that fuzz formation required $\sim 10^{24}$ m^{-2} in He fluence is important. To simulate the He fluence as same as experiments is impossible for MD because of the short elapse time of at most 1 μs. In general, the incident flux in experiments is in the range of $10^{20} - 10^{24}$ m^{-2}s^{-1}, while the incident flux in MD is often set to 10^{28} m^{-2}s^{-1} or higher. However, it is not recommended to choose the incident flux extremely higher than in the experiment, because the distribution of He bubbles should depend on the incident flux. When the incident flux is high, He atoms easily cluster in shallow areas, while when the incident flux is low, the He atoms diffuse deeply before clustering. Therefore, the ideal simulation is to achieve the He fluence as large as possible while using an incident flux close to experimental conditions.

One of the strategies for this problem is to use a high-performance computing (HPC). Hammond *et al.*[102–104] employed the MD with massively parallel computing. Their MD was able to reduce the incident flux to 10^{25} m^{-2}s^{-1} and to achieve 10^{19} m^{-2} in He fluence. On these realistic conditions, the dependence of the He bubble distribution on the incident flux was investigated in detail. Moreover, the size of pinholes due to He bubbles reached about 4 nm (see Fig. 15), which is larger than the size of pinholes just after the bursting mentioned above (< 1 nm). Namely, after the pinhole bursts, it takes a long time before it becomes large enough to be observed by an SEM.

In addition, a technical solution to achieve high helium fluence is the hybrid simulation of MD and KMC[105,106]. The diffusion and agglomeration of He atoms are solved fast by KMC on a grid system with a width of several Å, and the deformation of W material due to the high pressure of He bubbles is solved by MD. In the algorithm, KMC and MD are switched alternately at a regular interval. The hybrid simulation could achieve 10^{22} m^{-2} in the He fluence under the condition that the incident flux is 10^{22} m^{-2}s^{-1}, although it depends on the calculation time. In the simulation, it is needed to convert the data of atomic positions to the data of a discretized grid. The grid cell is classified into a W bulk cell, a He bubble cell, and a vacuum cell. For example, the region where a He bubble exists in MD is converted to a He bubble cell. When a He bubble bursts, the cell changes into a vacuum cell. In the KMC on these grid cells, He atoms can move on W cells. If a He atom reaches a vacuum cell, the He atom is vanished, which corresponds to the desorption of He atoms. If a He atom reached a He bubble cell, the He atom is regarded as trapped and then the He atom is added into the MD as an atomic particle. This hybrid simulation can treat swift processes of W atoms such as bursting and loop punching (∼10 ps/process). However, the slow processes of W atoms, such as thermal relaxation and surface diffusion, cannot be sufficiently represented. As a result, unfortunately, the hybrid simulation of MD and KMC can represent the formation of small surface roughness, but not enough for fuzz formation.

E. Normal Transport of Tungsten Atoms for Fuzz Growth

An unsolved problem for fuzz growth is the moving process of W atoms. In particular, it is not well understood what kind of mechanism causes the transport of W atoms in normal direction to the surface. Conversely, assuming the normal transport, it is possible to create a coarse-grained model for growth that has $\sqrt{t}$ dependence in the fuzz height. Lasa *et al.*[107] assume that the driving force of normal transport is a loop punching and rupture (bursting), and Martynenko[108] *et al.* assumed that the driving force is the gradient of W adatom concentration.

Here, let us consider that sputtering is also a candidate for the normal transport of W atoms. As mentioned in the section on the injection process, because the injection energy of He is lower than the sputtering threshold energy, it has been thought that sputtering hardly occurs. Therefore, in most simulations for slow deformations of W, such as the MD and hybrid simulations discussed in the previous subsection, He atoms are directly implanted into material without calculating the injection process. Another reason for avoiding the calculation of the injection process in MD is that the time step must be set short in order to handle fast-moving incident atoms, which requires a longer calculation time.

However, in the atomic scale viewpoint, the recoil cutoff energy E_{rc} to knock on a W atom is expected to generally decrease on rough surfaces compared with a bulk region, and then the sputtering can occur even in low incident energy. In order to treat the incident process, the above hybrid simulation has been extended to the BCA-MD-KMC hybrid simulation[109], in which the incident process is solved by using BCA in addition to MD for material deformation and KMC for helium diffusion. In a recent work[110], the hybrid simulation achieved the total fluence of 1.0×10^{24} m^{-2} under the flux of 1.4×10^{22} m^{-2}s^{-1}. As a result, the growth of the fiberform structure was represented as shown in Fig. 16.

A key point in the hybrid simulation is that E_{rc} is given by $E_{\mathrm{c}}\sqrt{n/8}$, where E_{c} is the cohesive energy of bulk and n is a coordination number for each atom. Namely, E_{rc} becomes smaller than E_{c} when n is smaller than the coordination number of bulk W, 8. From the MD part, n, which reflects the deformed material structure, is estimated. By this model, W atoms located at a rough surface can be sputtered by the He atom whose incident energy is 100 eV or less. Actually, the number of sputtering events was low when the surface was flat, while the number of sputtering events increased after the bursting of He bubbles made the surface rough. Some of the sputtered W atoms are re-deposited at the tips of the surface, and the net sputtering yield is kept low at $\sim 10^{-4}$. Finally, the height of the fiberform structure reached about 40 nm. At least in the hybrid simulation, the sputtering and the re-deposition were dominant mechanisms for the normal transport of W atoms. These mechanisms are consistent with the fact that deposition enhanced the LFN growth.

The other candidate of the normal transport is the effect called surface diffusion. The fundamental viewpoint of the surface diffusion is the migration of an adatom on flat surface[111]. From the comparison among the migration barrier energy[112,113], the diffusion of a W adatom on (110) surface is faster than the diffusion on other surface planes. From the estimation using MD[114], the migration barrier energy for a W adatom on (110) surface $\Delta E = 0.89$ eV and its pre-factor $D_0 = 6.92 \times 10^{-7}$ m^2/s, which does not seem to be slow. However, it should be noted that even if the diffusion of a single atom is fast, it will be clustered or trapped at the edge of steps. Then, the diffusion is slowed down, so that the adatoms on W surfaces are not moving permanently fast. In addition, it should be considered that the (110) surface does not dominate the surface of fuzz, which is winding in nanometer scale.

If adatoms are clustered quickly or trapped somewhere, what matters is the frequency of formation of adatoms. From the MD simulation[115], it seems that adatom can generate on the surface by increasing the concentration of He atoms in the shallow part of the surface. There is a possibility that the deposition of W atom is the cause of adatom formation. The sputtering and the re-deposition processes in the above hybrid simulation also can be regarded as the occurrence of the adatom formation. In growth of the LFN, aggressive deposition produces many adatoms.

However, it is difficult to even distinguish adatoms on rough surfaces, such as the surfaces of fuzz or the surfaces with bubbles burst. Then, it is probably appropriate to regard surface diffusion as a collective motion rather than as a migration of individual atoms. The statistical mechanical effects such as chemical potential[108] and the effects of macroscopic physical quantity such as stress[74,116] can also be important factors. For instance, Chen *et al.* demonstrated, using a continuity simulation and linear stability theory, that the stress induced by the high pressure of He bubbles in nano-scale tips causes a long-wavelength surface morphological instability, and then the fiberform nanostructure was generated[117]. Moreover, their model showed that a temperature influence and a He concentration influence on the incubation fluence, with the incubation fluence decreasing with increasing the temperature[118]. Here, the temperature dependence is the most interesting factor in fuzz growth and is often observed experimentally. However, atomic simulations from a microscopic viewpoint have too few degrees of freedom and to clearly show the temperature dependence in fuzz growth. Continuous models from a macroscopic viewpoint are essential in this respect. Thus, the growth factors of fuzz is not fully elucidated. Candidates for the normal transport of W atoms will continue to be proposed and discussed.

V. APPLICATIONS

The unique characteristic of the fuzz surface has various potential applications as functional materials. Here, we introduce two major candidate applications: gas sensor and photocatalysts.

A. Gas sensor

As mentioned earlier, the fuzz structure has a large surface area and a complex structure. Gas particles more likely to be trapped in the fuzzy structure than a flat surface. Plus, the surface reactions, mainly oxidation-reduction reactions, for gas detection are enhanced due to the different surface energies of the nano-size fibers. Thus, fuzz can be an ideal structure for the gas sensing application. The improved performance of the gas sensing has been firstly reported in Ref. 119 using fuzzy Mo oxide, and 20% improvement of the sensor response was confirmed for ethanol gas detection. Then, by optimizing the electrode and other parameters, a 500% improvement in sensor response has been confirmed for hydrogen gas detection using fuzzy W oxide[120], as shown in Fig. 19. The gas sensor with the fuzz structure can be prepared as follows (see Fig. 17). First, using a magnetron sputtering system, a metallic Mo or W film (∼500 nm) was deposited on a fused silica substrate. Second, by He plasma irradiation, fuzzy nanostructures were formed on the thin film surface. Third, by calcination under dry air in a tube furnace, the thin film with nanostructures was oxidized. And finally, a sensor sample can be prepared by depositing gold electrodes for electron resistance measurement using an electron beam evaporation system. The sensor response was examined by varying the concentration of the objective gas in dry air. The sensor sample was placed in the tube furnace and the ambient temperature was kept at a constant value. Using mass flow controllers, two gas cylinders, 100% dry air and standard gas containing a trace amount of hydrogen, ethanol, or ethylene, were switched or mixed to produce the desired concentration of the objective gas flow. The total gas flow was kept constant. The change in the resistance value between the surface electrodes was measured with a multimeter to examine the reactivity to the gas. Typical results are shown in Fig 18. The sensor response was evaluated by

$$\frac{R_{\mathrm{Air}} - R_{\mathrm{Gas}}}{R_{\mathrm{Air}}} \times 100(\%), \tag{3}$$

where R_{Air} is the base resistivity during the 100% dry air flow, and R_{Gas} is the resistivity during the objective gas flow. As Fig. 19 shows, the sensor response increases as the ambient temperature increases. However, as the temperature exceeds 350°C, the response slightly drops. In general, the conductance of the metal oxide semiconductors is a function of temperature. In the higher ambient temperature, R_{Air} gets smaller. Then, the value $R_{\mathrm{Air}} - R_{\mathrm{Gas}}$ and the sensor response become smaller. Thus, the sensor response has a peak at 300–350^{o}C for the WO_3 sensors. In addition to the operating temperature, the response was also improved by optimizing the oxidation temperature. A higher oxidation temperature causes a deeper oxidation. If oxidation is insufficient, the electric resistance becomes lower because some oxide (e.g. $WO_{2.72}$) is electrically conductive. With a lower electric resistance, the sensor response becomes smaller. The higher sensitivity of the fuzz sensors was confirmed by these studies.

For the gas sensor applications, there are three important “S”: Sensitivity, Selectivity, and Stability. To improve the selectivity, additional catalytic nanoparticles should be examined. Nanoparticles may improve a sticking coefficient of the target gas molecules and enhance the reaction. Nickel, Pt, Pd are the main candidates. If the sensitivity is well improved, it will improve the stability. With high-sensitive sensor materials, the sensor can be operated at lower temperatures, even at room temperature. In this case, the surface deformation is less likely and the stability is improved. In addition, operation at low temperatures is also beneficial for the power efficiency. For the universe of trillions of sensors, the power source is limited, thus low power gas sensors are essential.

B. Photocatalysts

Increases in the surface area and optical absorptance/absorbance by the formation of nanostructures on the surface is beneficial for photocatalysts[121]. Metals themselves cannot be photocatalysts; oxides of various metals such as V, Ti, Cr, zinc, tin, W, cerium are prosperous semiconductor photocatalysts[122].

1. *Tungsten trioxide*

Since fuzz was identified on W, two photocatalytic reactions are tested after oxidization, as far as we know: methylene blue (MB) ($C_{16}H_{18}N_3SCl$) decolorization reaction[66,123] and photoelectrochemical (PEC) characterization (photocurrent measurements)[124].

Figure 20(a) shows time courses of MB concentration as a function of light irradiation time using the setup shown in the inset of Fig. 20(a). A WO_3 sample was placed in 2 ml of aqueous MB solution (10 μmol/l) and exposed to visible light from a 300 W Xe lamp through an optical filter (long-pass optical filters with the edge wavelengths of 520 and 700 nm). It is noted that the decolorization progressed even though only near infrared light ($>$ 700 nm) was used for the irradiation. Concerning the MB decolorization, the surface oxidation fraction, which was measured by X-ray photoelectron spectroscopy (XPS), was an important factor. It was found that MB decolorization rate varied significantly with changing the oxidation fraction, and the reaction rate has a peak when the oxidation fraction was 60%[123]. The results suggested that the interface between W and WO_3 played an important role for the decolorization process. Also, oxygen vacancies, which are known to be influential factor for the photocatalytic performance, were found to be formed and stable in fuzzy WO_3[125].

Although the MB decolorization process is a simple method to measure the photocatalytic process, it is not easy to judge if the decolorization is due to the absorption or decomposition reaction. Komori *et al.* has revealed from S K-edge X-ray absorption near edge structure (XANES) analysis on both of the samples before and after the MB decolorization process that the MB molecules have been actually decomposed[126]. The σ^*(S-C) peak in the XANES spectra decreased and a new peak from SO_4^{2-} was identified after the light irradiation; the results suggested that NIR light irradiation breaks S-C bonds in a MB molecule and the sulfur species are formed in the state of SO_4^{2-} ion.

PEC performances have been measured using oxidized fuzzy W with an optimized two-step oxidation annealing procedure[124]. The sample showed five times greater photocurrent density than non-porous WO_3 sample from a W disc. Feng *et al.* investigated the PEC performance using oxidized fuzzy W with different h_{fuzz}[127] and optimized h_{fuzz} and oxidized temperature for the PEC performance. In the inset of Fig. 20(b), the setup for the PEC measurement is shown. A coiled Pt wire, an Ag/AgCl/sat. KCl electrode, and a prepared WO_3 sample were used as the counter electrode, the reference electrode (RE), and the working electrode, respectively, and a 0.5 M H_2SO_4 solution was used for the electrolyte. Linear sweep voltammetry curves were obtained under chopped incident light. In Fig. 20(b), it was found that WO_3 sample from a thin fuzz layer (15 min irradiation) W has higher performance than the one from thicker fuzz layer (30 min irradiation). It was discussed that recombination occurs before the produced electrons reach the conduction layer when h_{fuzz} is too thick.

One of the problems to be overcome is that the photocatalytic property decreases during the MB decomposition or PEC water splitting[123,127]. Because it was found the degradation rate could be changed by the oxidation procedure[123], it is necessary to optimize the structure and the oxidation process or put additional coating of thin film layer on the fuzzy surface[128].

2. Titanium dioxide

Titania (TiO_2) has been one of the most popular photocatalytic materials since the discovery of the Honda-Fujishima effect[129]. In addition to the water splitting, it has been used for various applications including air purification, sterilization, and cancer therapy[130].

After the fuzz growth condition on Ti has been revealed[131,132], photocatalytic performances have been investigated on He irradiated Ti samples via hydrogen production reaction from aqueous methanol solution and ethylene decomposition, which is necessary for the transportation and storage of horticultural crops[133]. For the hydrogen production reaction, a nanostructured sample has revealed roughly three times greater photocatalytic performance[134]. This can be explained by the increase in the active surface area. For the ethylene decomposition, various fabrication methods have been investigated including thin film deposition on W fuzz and Ti thin film fuzzy samples[128,135,136]. However, the effect of the increase in surface area did not appear clearly; rather, the performance seemed more sensitive to the crystal structure. It was shown that anatase structure, which is known to be more active than rutile, can be formed on He plasma exposed samples with high ethylene decomposition efficiency and is stable even at higher calcination temperatures (> 1000 K), though anatase is rarely formed on non-He-plasma-irradiated samples[136]. This suggested another aspect of He plasma irradiation effects in addition to the increase in surface area.

3. Iron oxides

Hematite (α-Fe_2O_3) is a semiconductor with the band gap energy of 2-2.2 eV and thought to be a promising material for oxygen evolution reaction (OER), which is a half-reaction to drive the water splitting[137]. Based on an investigation of He plasma irradiation effects on Fe thin films[138], PEC performance of oxidized nanostructured Fe thin film has been measured[139].

The photocurrent density on a plasma exposed thin film for 20 min (SE) had 2-5 times higher than that on an unexposed film (UE), while a clearly nanostructured film exposed to the plasma for 50 min (LE) had lower performance than SE. From the electrochemical impedance spectroscopy, it was shown that SE and LE had 10- and 40-times greater surface area than that of UE, respectively. Thus, the increase in the photocurrent density was less than the increase in the active surface area. It was discussed that the presence of defects including maghemite phase (Fe_3O_4) could act as the recombination center. Also, the roles of secondary elements such as Sn, Si and Zn, and the presence of maghemite (γ-Fe_2O_3) identified on UE have been discussed.

4. Others and summary

Helium plasma irradiation effects on the photocatalytic performances have been investigated on other metallic oxides. Methylene blue decomposition by UV light irradiation was performed using fuzzy niobium oxides (Nb_2O_5)[64]. Although no enhancement occurred on fuzzy samples, the performance increased with Pt support. Also, H_2 production from aqueous methanol solution using fuzzy vanadium oxides sample has been conducted, and it was shown that He plasma irradiation activated photocatalytic performance[140].

Dry processing can be used to form multiple thin film layers and add a small amount of novel metals such as Ag, Au and Pd. Further studies with the combination of He plasma irradiation and thin film deposition, which can be a novel method for the fabrication of nanostructured heterogeneous photocatalysts[141], are of interest. The He effect can also be beneficial in ways other than increasing surface area, such as the formation of stable anatase and oxygen vacancies. Fundamental understandings of the role of He implantation for photocatalytic materials are important.

VI. SUMMARY

In this tutorial, we presented and discussed the growth process and growth condition of fuzz on various metals including W based on experiments and simulation, and progresses on the application of fuzz-based materials. Currently, both experimental and simulation studies are being actively conducted including the formation mechanism of fuzz and their effects on fusion reactors. In the past decade, the effects on fusion reactors have gradually become clear. However, it has not yet been determined whether or not the formation will proceed in a fusion reactor, and further research is needed, in particular, with regard to the temperature increase, energy increase, and redeposition effects associated with Edge Localized Modes (ELMs). As detailed in Sections II and IV, the growth mechanism is gradually becoming clear. As described in Sec. II, the formation of NTBs with a height of tens of micrometers and LFNs with a thickness of mm have been found in recent years. The verification and modeling of these formation processes is important and may lead to a new aspect of the understanding of fuzz growth.

In addition to the problems in fusion reactors, the fact that fuzz growth occurs on various metals, as described in Sec. III, will greatly broaden the range of industrial applications. Enhanced performances in gas sensors and photocatalytic materials have been already demonstrated, as described in Sec. V. As for photocatalytic materials, various metal oxides, nitrides, and sulfides of tungsten, tantalum, niobium, and vanadium are expected to replace TiO_2 as visible light responsive photocatalysts[142], and it is important that cross-disciplinary research be further promoted. There is one hurdle in the process for industrial application research. With pure He plasma irradiation, a helium fluence of $10^{25} - 10^{26}$ m^{-2} is required for the fuzz growth to occur, and fuzz formation requires the use of devices that can generate high-density plasmas, such as divertor simulators. It has been reported that nanostructuring can also be performed in magnetron sputtering devices, but it requires about 10 hours of time. If fuzz can be formed simply and in a short time, the possibilities for industrial application research will increase. The selection and development of an optimal plasma source and the development of a device that can withstand mass production by making full use of accelerated fuzz growth by deposition, etc., as described in Sec. II, are future issues.

ACKNOWLEDGEMENT

One of the authors (S.K.) thanks Dr. M Tokitani and Prof. Sakamoto at National Institute for Fusion Science for useful dicussion about the crystal orientation dependence. This work was supported in part by a Grant-in-Aid for Scientific Research 19H01874, 19H01882, 19K21870 and 21K18617, and Fund for the Promotion of Joint International Research 17KK0132 from the Japan Society for the Promotion of Science (JSPS). A part of simulation is carried out on "Plasma Simulator" (NEC SX-Aurora TSUBASA) in NIFS with the support and under the auspices of the NIFS Collaboration Research program (NIFS22KISS027).

REFERENCES

[1] H. Iwakiri, K. Morishita and N. Yoshida: Journal of Nuclear Materials **307-311** (2002) 135.

[2] D. Nishijima, M. Ye, N. Ohno and S. Takamura: Journal of Nuclear Materials **329-333** (2004) 1029.

[3] S. Takamura, N. Ohno, D. Nishijima and S. Kajita: Plasma and Fusion Research **1** (2006) 051.

[4] S. Kajita, W. Sakaguchi, N. Ohno, N. Yoshida and T. Saeki: Nucl. Fusion **49** (2009) 095005.

[5] H. Iwakiri, K. Yasunaga, K. Morishita and N. Yoshida: Journal of Nuclear Materials **283-287** (2000) 1134.

[6] G. De Temmerman, K. Bystrov, J. J. Zielinski, M. Balden, G. Matern, C. Arnas and L. Marot: Journal of Vacuum Science & Technology A **30** (2012) 041306.

[7] D. Nishijima, M. Baldwin, R. Doerner and J. Yu: Journal of Nuclear Materials **415** (2011) S96.

[8] S. Kajita, Y. Tsuji and N. Ohno: Phys. Lett. A **378** (2014) 2533.

[9] M. Yajima, Y. Hatano, S. Kajita, J. Shi, M. Hara and N. Ohno: Journal of Nuclear Materials **438** (2013) S1142.

[10] S. Takamura, T. Miyamoto and N. Ohno: Fusion Science and Techology **63** (2013) 225.

[11] M. Patino, Y. Raitses and R. Wirz: Applied Physics Letters **109** (2016) 201602.

[12]S. Kajita, N. Ohno, Y. Hirahata and M. Hiramatsu: Fusion Engineering and Design **88** (2013) 2842.

[13]D. Hwangbo, S. Kajita, N. Ohno and D. Sinelnikov: IEEE Transactions on Plasma Science **45** (2017) 2080.

[14]S. Kajita, A. Ohta, T. Ishida, K. Makihara, T. Yoshida and N. Ohno: Japanese Journal of Applied Physics **54** (2015) 126201.

[15]S. Kajita, T. Yagi, K. Kobayashi, M. Tokitani and N. Ohno: Results in Physics **6** (2016) 877.

[16]S. Kajita, T. Saeki, N. Yoshida, N. Ohno and A. Iwamae: Applied Physics Express **3** (2010) 085204.

[17]S. Kajita, N. Ohno, T. Yokochi, N. Yoshida, R. Yoshihara, S. Takamura and T. Hatae: Plasma Physics and Controlled Fusion **54** (2012) 105015.

[18]D. Nishijima, Y.Kikuchi, M. Nakatsuka, M. Baldwin, R. Doerner, M. Nagata and Y. Ueda: Fusion Science and Technology **60** (2011) 1447.

[19]S. Kajita, S. Takamura, N. Ohno, D. Nishijima, H. Iwakiri and N. Yoshida: Nucl. Fusion **47** (2007) 1358.

[20]S. Kajita, G. D. Temmerman, T. Morgan, S. van Eden, T. de Kruif and N. Ohno: Nuclear Fusion **54** (2014) 033005.

[21]S. Kajita, S. Takamura and N. Ohno: Nucl. Fusion **49** (2009) 032002.

[22]M. Tokitani, S. Kajita, S. Masuzaki, Y. Hirahata, N. Ohno, T. Tanabe and LHD Experiment Group: Nucl. Fusion **51** (2011) 102001.

[23]S. Kajita, D. Hwangbo and N. Ohno: IEEE Transactions on Plasma Science **47** (2019) 3609.

[24]Y. Gasparyan, V. Efimov and K. Bystrov: Nuclear Fusion **56** (2016) 054002.

[25]T. Petty, M. Baldwin, M. Hasan, R. Doerner and J. Bradley: Nuclear Fusion **55** (2015) 093033.

[26]M. Baldwin and R. Doerner: Nucl. Fusion **48** (2008) 035001 (5pp).

[27]M. Baldwin, R. Doerner, D. Nishijima, K. Tokunaga and Y. Ueda: Journal of Nuclear Materials **390-391** (2009) 886.

[28]T. Petty and J. Bradley: Journal of Nuclear Materials **453** (2014) 320.

[29]T. Petty, A. Khan, T. Heil and J. Bradley: Journal of Nuclear Materials **480** (2016) 374.

[30] N. Ohno, Y. Hirahata, M. Yamagiwa, S. Kajita, M. Takagi, N. Yoshida, R. Yoshihara, T. Tokunaga and M. Tokitani: Journal of Nuclear Materials **438, Supplement** (2013) S879.

[31] C. Parish, H. Hijazi, H. Meyer and F. Meyer: Acta Materialia **62** (2014) 173.

[32] S. Kajita, N. Yoshida, N. Ohno, Y. Hirahata and R. Yoshihara: Physica Scripta **89** (2014) 025602.

[33] R. Sakamoto, E. Bernard, A. Kreter and N. Yoshida: Nuclear Fusion **57** (2017) 016040.

[34] R. Sakamoto, E. Bernard, A. Kreter, C. Martin, B. Pégourié, G. Pieters, B. Rousseau, C. Grisolia and N. Yoshida: Physica scripta **2017** (2017) 014062.

[35] C. M. Parish, K. Wang, R. P. Doerner and M. J. Baldwin: Scripta Materialia **127** (2017) 132.

[36] S. Kajita, T. Nojima, T. Okuyama, Y. Yamamoto, N. Yoshida and N. Ohno: Acta Materialia **181** (2019) 342.

[37] F. Ferroni, K. D. Hammond and B. D. Wirth: Journal of Nuclear Materials **458** (2015) 419.

[38] R. Doerner, M. Baldwin and P. Stangeby: Nucl. Fusion **51** (2011) 043001.

[39] Y. Noiri, S. Kajita and N. Ohno: Journal of Nuclear Materials **463** (2015) 285.

[40] A. Kirschner, D. Tskhakaya, S. Brezinsek, D. Borodin, J. Romazanov, R. Ding, A. Eksaeva and C. Linsmeier: Plasma Physics and Controlled Fusion **60** (2017) 014041.

[41] M. Baldwin and R. Doerner: Journal of Nuclear Materials **404** (2010) 165.

[42] S. Takamura and T. Miyamoto: Plasma and Fusion Research **6** (2011) 1202005.

[43] S. Kajita, N. Yoshida, R. Yoshihara, N. Ohno, T. Yokochi, M. Tokitani and S. Takamura: Journal of Nuclear Materials **421** (2012) 22.

[44] G. D. Temmerman, R. Doerner and R. Pitts: Nuclear Materials and Energy **19** (2019) 255 .

[45] S. Kajita, N. Ohno, M. Yajima and J. Kato: Journal of Nuclear Materials **440** (2013) 55.

[46] K. Woller, D. Whyte and G. Wright: Nuclear Fusion **57** (2017) 066005.

[47] D. Hwangbo, S. Kajita, N. Ohno, P. McCarthy, J. W. Bradley and H. Tanaka: Nuclear Fusion **58** (2018) 096022.

[48] A. Al-Ajlony, J. Tripathi and A. Hassanein: Journal of Nuclear Materials **466** (2015) 569.

[49] K. B. Woller, D. G. Whyte and G. M. Wright: Journal of Applied Physics **129** (2021) 115301.

[50]D. Sinelnikov, D. Bulgadaryan, D. Hwangbo, S. Kajita, V. Kurnaev and N. Ohno: IEEE Transactions on Plasma Science **47** (2019) 5186.

[51]S. Kajita, M. Fukumoto, M. Tokitani, T. Nakano, Y. Noiri, N. Ohno, S. Masuzaki, S. Takamura, N. Yoshida and Y. Ueda: Nuclear Fusion **53** (2013) 053013.

[52]S. Kajita, S. Kawaguchi, N. Ohno and N. Yoshida: Sci. Rep. **8** (2018) 56.

[53]P. McCarthy, D. Hwangbo, M. Bilton, S. Kajita and J. W. Bradley: Nuclear Fusion **60** (2020) 026012.

[54]S. Kajita, T. Morgan, H. Tanaka, Y. Hayashi, N. Yoshida, D. Nagata, J. Vernimmen, S. Feng, R. Zhang and N. Ohno: Journal of Nuclear Materials **548** (2021) 152844.

[55]W. Shen, S. Kajita, H. Tanaka, Q. Shi and N. Ohno: Plasma and Fusion Research **17** (2022) 1302094.

[56]S. Kajita, S. Kawaguchi, N. Yoshida, N. Ohno and H. Tanaka: Nucl. Fusion **58** (2018) 106002.

[57]W. Boettinger, G. McFadden, S. Coriell, R. Sekerka and J. Warren: Acta Materialia **53** (2005) 1995.

[58]A. Khan, G. De Temmerman, T. W. Morgan and M. B. Ward: Journal of Nuclear Materials **474** (2016) 99.

[59]R. Doerner, D. Nishijima, S. Krasheninnikov, T. Schwarz-Selinger and M. Zach: Nuclear Fusion **58** (2018) 066005.

[60]P. Fiflis, N. Connolly and D. Ruzic: Journal of Nuclear Materials **482** (2016) 201.

[61]T. Nojima, S. Kajita, N. Yoshida, S. Kawaguchi, N. Ohno, H. Tanaka, M. Tokitani, D. Nagata, T. Akiyama and T. Yagi: Plasma and Fusion Research **13** (2018) 3406065.

[62]K. Omori, A. M. Ito, K. Shiga, N. Yamashita, K. Ibano, H. T. Lee and Y. Ueda: Journal of Applied Physics **121** (2017) 155301.

[63]Y. Ueda, N. Yamashita, K. Omori, H. Lee, K. Ibano and A. Ito: Journal of Nuclear Materials **511** (2018) 605.

[64]S. Kajita, F. Mimuro, T. Yoshida, N. Ohno and N. Yoshida: ChemPhysChem **19** (2018) 3237.

[65]S. Kajita, T. Nojima, Y. Tomita, N. Ohno, H. Tanaka, N. Yoshida, M. Yajima, T. Akiyama, M. Tokitani and T. Yagi: Surface and Coatings Technology **340** (2018) 86.

[66]S. Kajita, T. Yoshida, D. Kitaoka, R. Etoh, M. Yajima, N. Ohno, H. Yoshida, N. Yoshida and Y. Terao: Journal of Applied Physics **113** (2013) 134301.

[67]S. Kajita, T. Nojima, Y. Yamamoto, N. Yoshida, T. Okuyama, T. Kuwabara and N. Ohno: Japanese Journal of Applied Physics **59** (2020) SHHA03.

[68]R. Doerner, M. Baldwin and D. Nishijima: Journal of Nuclear Materials **455** (2014) 1.

[69]D. Nishijima, A. Kreter, M. Baldwin, D. Borodin, A. Eksaeva, D. Hwangbo, S. Kajita, M. Miyamoto, N. Ohno, M. Patino, A. Pospieszczyk, M. Rasinski, T. Schlummer, A. Terra and R. Doerner: Nuclear Materials and Energy **18** (2019) 67.

[70]Q. Shi, S. Kajita, N. Ohno, M. Tokitani, D. Nagata and S. Feng: Journal of Applied Physics **128** (2020) 023301.

[71]Q. Shi, S. Kajita, S. Feng and N. Ohno: Journal of Physics D: Applied Physics **54** (2021) 405202.

[72]S. Kajita, T. Ishida, N. Ohno, D. Hwangbo and T. Yoshida: Sci. Rep. **6** (2016) 30380.

[73]J. H. Evans: Journal of Nuclear Materials **334** (2004) 40.

[74]S. I. Krasheninnikov: Physica Scripta **2011** (2011) 014040.

[75]R. Smirnov and S. Krasheninnikov: Nuclear Fusion **53** (2013) 082002.

[76]S. Takamura and Y. Uesugi: Applied Surface Science **356** (2015) 888.

[77]B. D. Wirth, K. Hammond, S. Krasheninnikov and D. Maroudas: Journal of Nuclear Materials **463** (2015) 30.

[78]J. P. Biersack and W. Eckstein: Applied Physics **A34** (1984) 73.

[79]W. Eckstein, *Computer Simulation of Ion-Solid Interactions, Springer Series in Materials Science* (Springer-Verlag, Berlin Heidelberg, 1991).

[80]W. Eckstein: Radiation Effects and Defects in Solids (1994) 239.

[81]W. Takeuchi and Y. Yamamura: Nuclear Instruments and Methods in Physics Research Section B: Beam Interactions with Materials and Atoms **2** (1984) 336.

[82]Y. Yamamura and Y. Mizuno: Institute of Plasma Physics, Nagoya University **IPPJ-AM-40** (1985) .

[83]T. Takizuka and H. Abe: Journal of Computational Physics **25** (1977) 205.

[84]A. Takayama, S. Saito, A. M. Ito, T. Kenmotsu and H. Nakamura: Japanese Journal of Applied Physics **50** (2011) 01AB03.

[85]S. Saito, A. Takayama, A. M. Ito and H. Nakamura: Journal of Nuclear Materials **438** (2013) S895.

[86]H. Nakamura, S. Saito, A. M. Ito and A. Takayama: Plasma and Fusion Research **11** (2016) 2401080.

[87] T. Klaver, S. Zhang and K. Nordlund: Journal of Nuclear Materials **492** (2017) 113.

[88] Z. Yang, W. Song, Y. Li and J. Yang: Nuclear Instruments and Methods in Physics Research Section B: Beam Interactions with Materials and Atoms **455** (2019) 118.

[89] C. Becquart and C. Domain: Journal of Nuclear Materials **386-388** (2009) 109, fusion Reactor Materials.

[90] A. Takayama, A. M. Ito, S. Saito, N. Ohno and H. Nakamura: Japanese Journal of Applied Physics **52** (2013) 01AL03.

[91] T. Tamura, R. Kobayashi, S. Ogata and A. M. Ito: Modelling Simul. Mater. Sci. Eng. **22** (2014) 015002.

[92] K. Omori, A. Ito, I. Mun, N. Yamashita, K. Ibano, H. Lee and Y. Ueda: Nuclear Materials and Energy **16** (2018) 226.

[93] F. Sefta, K. D. Hammond, N. Juslin and B. D. Wirth: Nuclear Fusion **53** (2013) 073015.

[94] R. Kobayashi, T. Hattori, T. Tamura and S. Ogata: Journal of Nuclear Materials **463** (2015) 1071.

[95] K. Henriksson, K. Nordlund and J. Keinonen: Nuclear Instruments and Methods in Physics Research Section B: Beam Interactions with Materials and Atoms **244** (2006) 377.

[96] A. M. Ito, Y. Yoshimoto, S. Saito, A. Takayama and H. Nakamura: Physica Scripta **2014** (2014) 014062.

[97] C. S. Becquart and C. Domain: Phys. Rev. Lett. **97** (2006) 196402.

[98] H. Eyring: The Journal of Chemical Physics **3** (1935) 107.

[99] K. Heinola and T. Ahlgren: Journal of Applied Physics **107** (2010) 113531.

[100] Y. Zhou, J. Wang, Q. Hou and A. Deng: Journal of Nuclear Materials **446** (2014) 49.

[101] A. M. Ito, S. Kato, A. Takayama and H. Nakamura: Nuclear Materials and Energy **12** (2017) 353.

[102] K. D. Hammond, S. Blondel, L. Hu, D. Maroudas and B. D. Wirth: Acta Materialia **144** (2018) 561.

[103] K. D. Hammond, I. V. Naeger, W. Widanagamaachchi, L.-T. Lo, D. Maroudas and B. D. Wirth: Nuclear Fusion **59** (2019) 066035.

[104] K. D. Hammond, B. F. Lee, I. V. Naeger, W. Widanagamaachchi, L.-T. Lo, D. Maroudas and B. D. Wirth: Nuclear Fusion **60** (2020) 129401.

[105] A. M. Ito *et al.*: Journal of Nuclear Materials **463** (2015) 109.

[106] A. Ito *et al.*: Nuclear Fusion **55** (2015) 073013.

[107] A. Lasa, S. K. Tahtinen and K. Nordlund: EPL (Europhysics Letters) **105** (2014) 25002.

[108] Y. V. Martynenko and M. Y. Nagel: Plasma Physics Reports **38** (2012) 996.

[109] A. M. Ito, A. Takayama and H. Nakamura: Plasma and Fusion Research **13** (2018) 3403061.

[110] A. M. ITO, A. TAKAYAMA and H. NAKAMURA, *Incident Energy Dependence of Tungsten Fuzzy Nanostructure Growth with BCA-MD-KMC Multi-Hybrid Simulation,* 2020, in Proceedings of 4th Asia-Pacific Conference on Plasma Physics.

[111] T. T. Tsong: Progress in Surface Science **67** (2001) 235.

[112] Z. Chen and N. Ghoniem: Phys. Rev. B **88** (2013) 035415.

[113] Q. Yang, Y.-W. You, L. Liu, H. Fan, W. Ni, D. Liu, C. S. Liu, G. Benstetter and Y. Wang: Scientific Reports **5** (2015) 10959.

[114] D. Chen, W. Hu, J. Yang, H. Deng, L. Sun and F. Gao: The European Physical Journal B **68** (2009) 479.

[115] K. D. Hammond and B. D. Wirth: Journal of Applied Physics **116** (2014) 143301.

[116] D. Dasgupta, R. D. Kolasinski, R. W. Friddle, L. Du, D. Maroudas and B. D. Wirth: Nuclear Fusion **59** (2019) 086057.

[117] C.-S. Chen, D. Dasgupta, R. D. Kolasinski, B. D. Wirth and D. Maroudas: Phys. Rev. Materials **5** (2021) 113403.

[118] C.-S. Chen, D. Dasgupta, A. Weerasinghe, B. D. Wirth and D. Maroudas: Nuclear Fusion **61** (2020) 016016.

[119] K. Ibano, Y. Kimura, T. Sugahara, H. T. Lee and Y. Ueda: Japanese Journal of Applied Physics **57** (2018) 040316.

[120] Y. Kimura, K. Ibano, K. Uehata, I. Hirai, H. Tae Lee and Y. Ueda: Applied Surface Science **532** (2020) 147274.

[121] C. Xu, P. Ravi Anusuyadevi, C. Aymonier, R. Luque and S. Marre: Chem. Soc. Rev. **48** (2019) 3868.

[122] M. M. Khan, S. F. Adil and A. Al-Mayouf: Journal of Saudi Chemical Society **19** (2015) 462, special Issue: Nanomaterials as Photocatalysts.

[123] K. Komori, T. Yoshida, S. Yagi, H. Yoshida, M. Yajima, S. Kajita and N. Ohno: e-J. Surf. Sci. Nanotech. **12** (2014) 343.

[124] M. de Respinis, G. De Temmerman, I. Tanyeli, M. C. van de Sanden, R. P. Doerner, M. J. Baldwin and R. van de Krol: ACS Applied Materials & Interfaces **5** (2013) 7621.

[125] S. Feng, S. Kajita, T. Yoshida, N. Ohno, D. Nagata and M. Tokitani: Materials Research Express **7** (2020) 075007.

[126] K. Komori, T. Yoshida, T. Nomoto, M. Yamamoto, C. Tsukada, S. Yagi, M. Yajima, S. Kajita and N. Ohno: Nuclear Instruments and Methods in Physics Research Section B: Beam Interactions with Materials and Atoms **365, Part A** (2015) 35.

[127] S. Feng, S. Kajita, M. Higashi, A. Bieberle-Hutter, T. Yoshida and N. Ohno: Applied Surface Science **580** (2022) 151979.

[128] Y. Tomita, S. Kajita, E. Yasunaga, T. Yoshida, N. Ohno and H. Tanaka: Japanese Journal of Applied Physics **58** (2019) SEEG01.

[129] A. Fujishima and K. Honda: Nature **238** (1972) 5358.

[130] A. Fujishima, T. N. Rao and D. A. Tryk: Journal of Photochemistry and Photobiology C: Photochemistry Reviews **1** (2000) 1.

[131] S. Kajita, D. Kitaoka, N. Ohno, R. Yoshihara, N. Yoshida and T. Yoshida: Applied Surface Science **303** (2014) 438.

[132] K. Miyaguchi, S. Kajita, H. Tanaka and N. Ohno: Japanese Journal of Applied Physics **60** (2021) 038004.

[133] N. Keller, M.-N. Ducamp, D. Robert and V. Keller: Chemical Reviews **113** (2013) 5029, pMID: 23590210.

[134] S. Kajita, T. Yoshida, N. Ohno, T. Ishida and D. Kitaoka: Japanese Journal of Applied Physics **55** (2016) 106202.

[135] S. Kajita, Y. Tomita, E. Yasunaga, T. Yoshida, K. Miyaguchi, H. Tanaka and N. Ohno: Japanese Journal of Applied Physics **58** (2019) 070903.

[136] S. Kajita, K. Miyaguchi, H. Tanaka, E. Yasunaga, T. Yoshida and N. Ohno: Journal of Photochemistry and Photobiology A: Chemistry **418** (2021) 113420.

[137] Y. W. Phuan, W.-J. Ong, M. N. Chong and J. D. Ocon: Journal of Photochemistry and Photobiology C: Photochemistry Reviews **33** (2017) 54.

[138] A. Bieberle-Hütter, I. Tanyeli, R. Lavrijsen, B. Koopmans, R. Sinha and M. van de Sanden: Thin Solid Films **631** (2017) 50.

[139] R. Sinha, I. Tanyeli, R. Lavrijsen, M. van de Sanden and A. Bieberle-Hütter: Electrochimica Acta **258** (2017) 709.

[140] S. Kajita, T. Yoshida, N. Ohno, Y. Ichino and N. Yoshida: Journal of Physics D: Applied Physics **51** (2018) 215201.

[141] J.-M. Herrmann: Catalysis Today **53** (1999) 115.

[142] A. Kudo and Y. Miseki: Chemical Society Reviews **38** (2009) 253.

[143] S. Kajita, T. Saeki, Y. Hirahata, M. Yajima, N. Ohno, R. Yoshihara and N. Yoshida: Jpn. J. Appl. Phys. **50** (2011) 08JG01.

[144] S. Kajita, N. Yoshida and N. Ohno: Nuclear Materials and Energy **25** (2020) 100828.

[145] S. Kajita, N. Yoshida, R. Yoshihara, N. Ohno and M. Yamagiwa: Journal of Nuclear Materials **418** (2011) 152.

[146] T. W. Morgan, M. Balden, T. Schwarz-Selinger, Y. Li, T. H. Loewenhoff, M. Wirtz, S. Brezinsek and G. D. Temmerman: Physica Scripta **T171** (2020) 014065.

[147] H. J. Monkhorst and J. D. Pack: Phys. Rev. B **13** (1976) 5188.

[148] J. P. Perdew, K. Burke and M. Ernzerhof: Phys. Rev. Lett. **77** (1996) 3865.

FIG. 1. (a,b) Cross sectional SEM micrographs of W fiberform nanostructures. The surface temperature during the irradiation, incident ion energy and helium fluence are 1700 K, 50 eV, and 2×10^{26} m^2, respectively. The helium irradiation was performed in the NAGDIS-I. (Reproduced with permission from S. Kajita *et al.*, Jpn. J. Appl. Phys. **50**, 08JG01 (2011). Copyright 2011 The Japan Society of Applied Physics.) and (c) Transmission electron microscope (TEM) micrograph of a fraction of W fuzz. Reproduced with permission from S. Kajita *et al.*, Nucl. Fusion **47**, 1358 (2007). Copyright 2007 IAEA.

FIG. 2. (a) Number of fuzz related publications (*fuzz* and *helium* in article contents) in each year from the year 2010 to 2021 and (b) number of fuzz related publications per journal (Scopus database).

FIG. 3. Cross-sectional TEM images of the nanostructured tungsten. The helium fluences are (a) 0.6×10^{25}, (b) 1.1×10^{25}, (c) 1.8×10^{25}, (d) 2.4×10^{25}, and (e) 5.5×10^{25} m^{-2}. The surface temperature is 1400 K and the incident ion energy is 50 eV. (Reproduced with permission from S. Kajita *et al.*, Appl. Phys. Express **3**, 085204 (2010). Copyright 2010 The Japan Society of Applied Physics.)

FIG. 4. A schematic of the fuzz growth process.

FIG. 5. The surface temperature was plotted as a function of the incident ion energy for helium irradiation experiments conducted in the divertor simulator NAGDIS-II and PISCES-B. Closed markers represent the cases in which the nanostructure was formed, while open markers represent the cases where the nanostructure was not observed. (Reproduced with permission from S. Kajita *et al.*, Nucl. Fusion **49**, 095005 (2009). Copyright 2009 IAEA.)

FIG. 6. Fuzz layer thickness versus He ion fluence. Indicated, ‘c’ labels refer to corrected values including the effect of erosion. The dashed line is related to the $t^{1/2}$ growth dependence. The full line accommodates the effect of an incubation fluence of $\Phi_{\mathrm{He},0} = 2.5 \times 10^{24}$ m^{-2}. Reproduced with permission from T. Petty *et al.*, Nucl. Fusion **55**, 093033 (2015). Copyright 2015 IAEA.

FIG. 7. SEM micrographs of crystal grains having crystal orientation of (a) {101}, (b) {001}, (c) {112}, (d) {111}, (e) {103}, (f) {102}, (g) {407} and (h) {203}. The irradiation condition is as follows: T_s of 1700 K, E_i of 25 eV, and Φ_{He} of 5.6×10^{26} m^{-2}. (Reproduced with permission from N. Ohno *et al.*, J. Nucl. Mat. **438**, S879 (2013). Copyright 2013 Elsevier.)

FIG. 8. SEM micrographs of NTBs grown in NAGDIS-II. (S. Kajita *et al.*, Nucl. Mat. Energy **25**, 100828 (2020); licensed under a Creative Commons Attribution-NonCommercial-NoDerivs (CC BY-NC-ND) license.)

FIG. 9. (a) An optical microscope image and (b) an SEM micrograph of W large-scale fuzz structures (LFNs). (S. Kajita *et al.*, Sci. Rep. **8**, 56 (2018); licensed under a Creative Commons (CC BY) license.)

FIG. 10. A summary of thickness of nanostructured layer as a function of He fluence: conventional fuzzy layer thickness without W deposition from NAGDIS-II[145], PISCES-B[25], and Magnum-PSI[146], the fuzzy layer thickness with auxiliary W deposition in Magnum-PSI[54] and a magnetron sputtering device[53], height of NTBs[46,47], initial growth phase of LFNs[56], and thickness of LFNs in the latter growth phase[52].

FIG. 11. SEM images of He plasma-irradiated nanostructures on various metal surfaces (Ti[131], Fe[66], Mo[62], Nb[64], Ta[72], and unpublished Pd and Ag micrographs were added to the original figure in Ref. 63). The irradiation to Pd and Ag were performed in the same ECR plasma device used in Ref. 63. The irradiation conditions were as follows: T_s of 548 K, E_i of 80 eV, and Φ_{He} of $\sim 4\times 10^{25}$ m^{-2} for Pd and T_s of 335 K, E_i of 120 eV, and Φ_{He} of $\sim 4\times 10^{25}$ m^{-2} for Ag. (Reproduced with permission from S. Kajita *et al.*, Appl. Surf. Sci. **303**, 438 (2014). Copyright 2014 Elsevier. Reproduced from S. Kajita *et al.*, J. Appl. Phys. **113**, 134301 (2013), with the permission of AIP Publishing. Reproduced from K. Omori *et al.*, J. Appl. Phys. **121**, 155301 (2017), with the permission of AIP Publishing. Reproduced with permission from S. Kajita *et al.*, ChemPhysChem **19**, 3237 (2018). Copyright 2018 Wiley. S. Kajita *et al.*, Sci. Rep. **6**, 30380 (2016); licensed under a Creative Commons (CC BY) license. Reproduced with permission from Y. Ueda *et al.*, J. Nucl. Mat. **511**, 605 (2018). Copyright 2018 Elsevier.)

FIG. 12. (a) The surface temperature during He irradiation where the fuzz growth occurred as a function of the melting point T_m. Dotted lines correspond to T_s/T_m=0.6 and 0.25. (b) The morphology changes presented using different markers and plotted as a function of the shear modulus and the melting point. The shear modulus is the averaged value between 0.25 T_m and 0.5 T_m, the error bars represent the maximum and minimum values. (Reproduced with permission from S. Kajita *et al.*, Surf. Coat. Technol. **340**, 86 (2018). Copyright 2018 Elsevier.)

FIG. 13. Multi-processes from helium irradiation to fuzz growth. Light and dark gray spheres indicate He and W atoms, respectively.

FIG. 14. The binding energies of He atoms in W, Mo, Cr, Ta, Nb, V and Fe, which have a BCC materials structure composed of 128 atoms of 4 × 4 × 4 super cells. (a) The agglomeration of He atoms at an interstitial site. (b) The agglomeration of He atoms at a mono-vacancy at which one metallic atom is removed from the BCC structure. In addition, the cross marks with black dashed line indicate the binding energy of H atoms at a mono-vacancy in W. DFT calculations were performed under the conditions that the Brillouin zone of 4 × 4 × 4 k-points was sampled with the Monkhorst-Pack[147] method and the generalized gradient approximation (GGA) with Perdew-Burke-Ernzerhof (PBE) functional[148] was used for exchange-correlation potential. The definition of the binding energies follows Refs. 90 and 92.

FIG. 15. Helium bubble formation in long-time simulations by massively parallel MD. Helium plasma is irradiated onto the tungsten W(001) surface at 100 eV. The incident flux is 4.94×10^{27} $\mathrm{m^{-2}s^{-1}}$ and the He fluence is 1.258×10^{21} $\mathrm{m^{-2}}$. In the left-hand image of top view, the color means the relative height from the original surface. The white, blue, red regions indicate the original surface, 3.5 nm below the original surface, and 3.5 nm above the original surface, respectively. In the right-hand figure of side view, black and gold regions indicate He bubbles and surfaces/voids, respectively (Reproduced with permission from K. Hammond *et al.*, Nucl. Fusion **60**, 129401 (2020). Copyright 2020 IAEA.)

FIG. 16. The fiber form nanostructure represented by the BCA-MD-KMC hybrid simulation[109] under the conditions that the incident He flux is 1.4×10^{22} $\mathrm{m^{-2}s^{-1}}$, the material temperature is 1100 K and the diffusivity of He atom in a KMC part is 1.0×10^{-8} $\mathrm{m^2s^{-1}}$. The incident He fluences correspond to (a) 1.4×10^{21} $\mathrm{m^{-2}}$, (b) 7.0×10^{22} $\mathrm{m^{-2}}$, and (c) 1.0×10^{24} $\mathrm{m^{-2}}$, respectively[110]. The spheres of atoms are drawn by the Jet color which indicates the height from the original surface in z direction.

FIG. 17. Schematic diagram of the gas sensor formation with fuzz surface (Reproduced with permission from Y. Kimura *et al.*, Appl. Surf. Sci. **532**, 147274 (2020). Copyright 2020 Elsevier.)

FIG. 18. Response curve of the 350°C annealing W oxide fuzz sample at 250 to 400°C operating temperature (Reproduced with permission from Y. Kimura *et al.*, Appl. Surf. Sci. **532**, 147274 (2020). Copyright 2020 Elsevier.)

FIG. 19. Response of tungsten oxide gas sensors to 100 ppm hydrogen as a function of the operating ambient temperature. Black circle and red triangle marks show fuzzy tungsten sensor with different annealing temperature, and green triangle marks show plane tungsten sensor. (Reproduced with permission from Y. Kimura *et al.*, Appl. Surf. Sci. **532**, 147274 (2020). Copyright 2020 Elsevier.)

FIG. 20. (a) Time courses of the MB concentration in aqueous solution with the samples under the photoirradiation of NIR light and (b) photocurrent density vs. applied potential curves under chopped light with W samples with no plasma irradiation, 15 min plasma irradiation, and 30 min plasma irradiation. All the samples were oxidized in an electric furnace at 773 K for 30 min. (Reproduced from S. Kajita *et al.*, J. Appl. Phys. **113**, 134301 (2013), with the permission of AIP Publishing. Reproduced with permission from S. Feng *et al.*, Appl. Surf. Sci. **580**, 151979 (2022). Copyright 2022 Elsevier.)

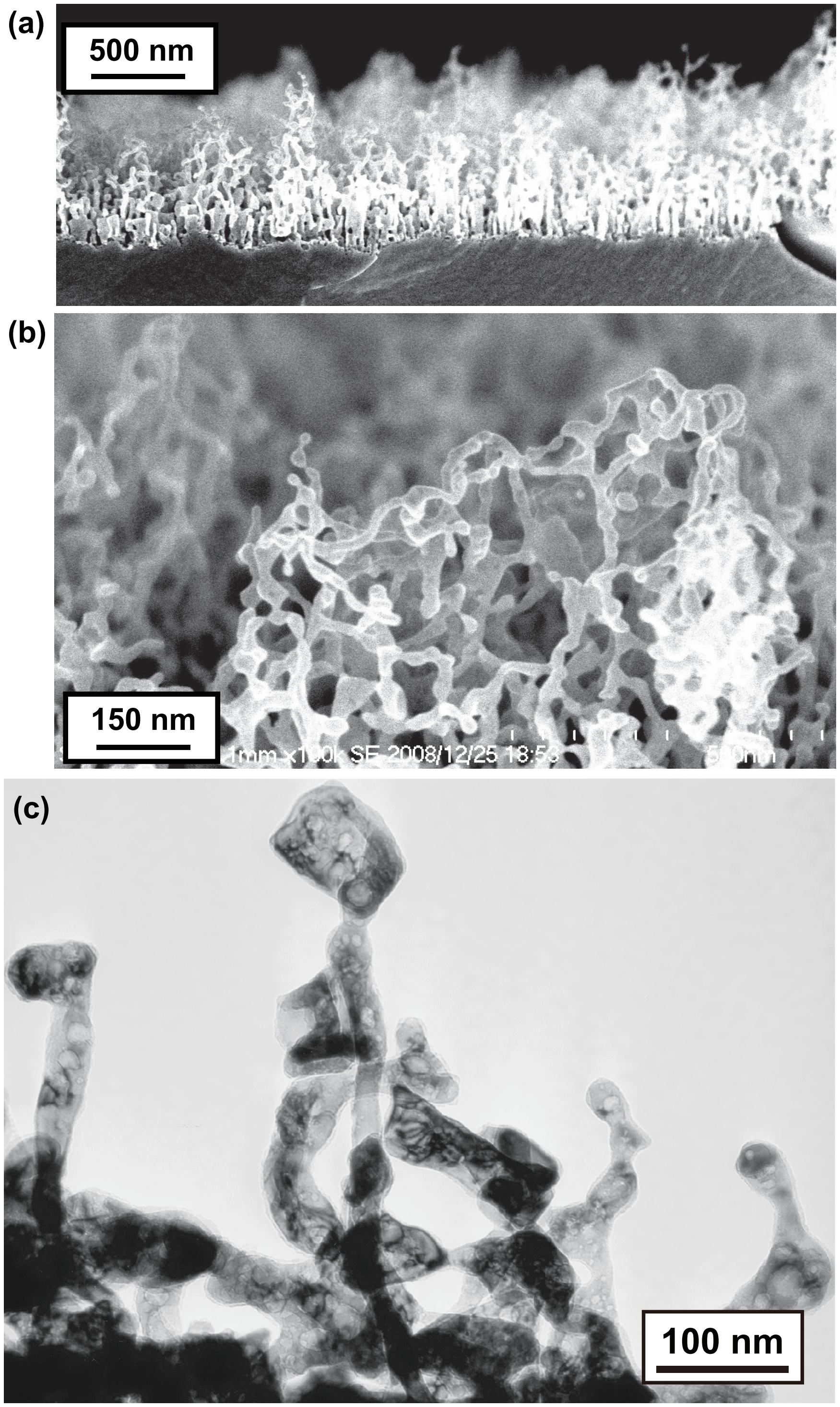
(a)
500 nm
(b)
150 nm
x100k SE 2008/12/25
(c)
100 nm

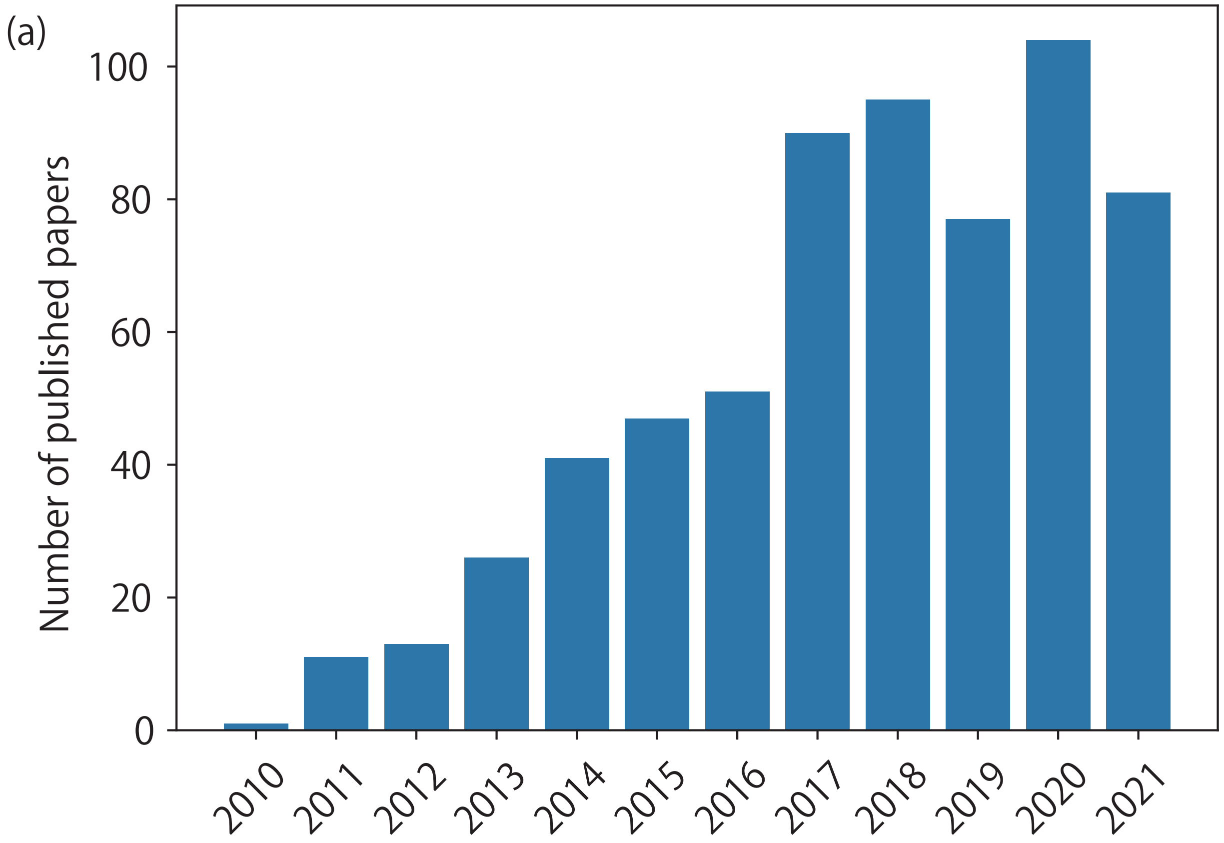
(a)
Number of published papers
0
20
40
60
80
100
2010
2011
2012
2013
2014
2015
2016
2017
2018
2019
2020
2021

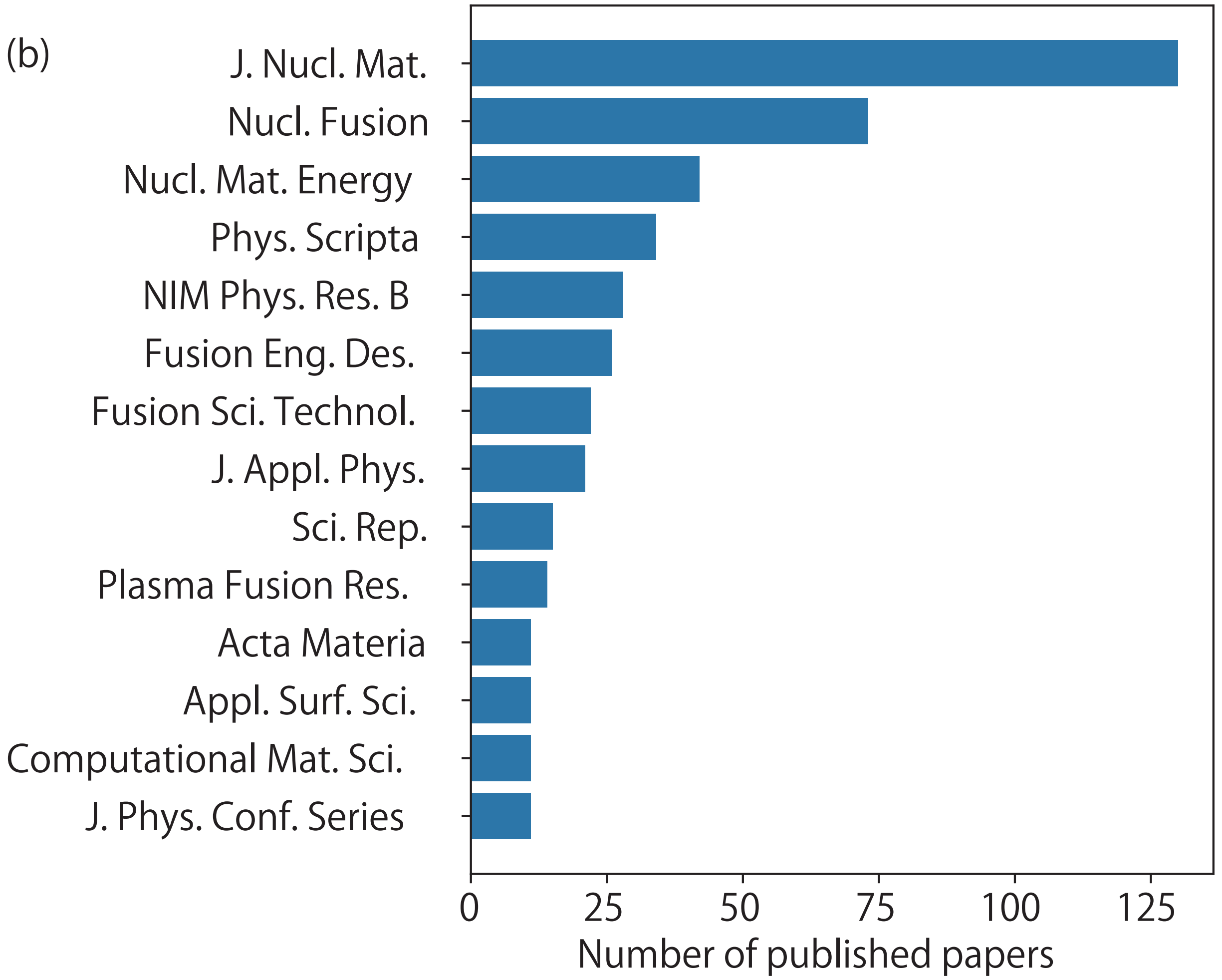
(b)
J. Nucl. Mat.
Nucl. Fusion
Nucl. Mat. Energy
Phys. Scripta
NIM Phys. Res. B
Fusion Eng. Des.
Fusion Sci. Technol.
J. Appl. Phys.
Sci. Rep.
Plasma Fusion Res.
Acta Materia
Appl. Surf. Sci.
Computational Mat. Sci.
J. Phys. Conf. Series
0
25
50
75
100
125
Number of published papers

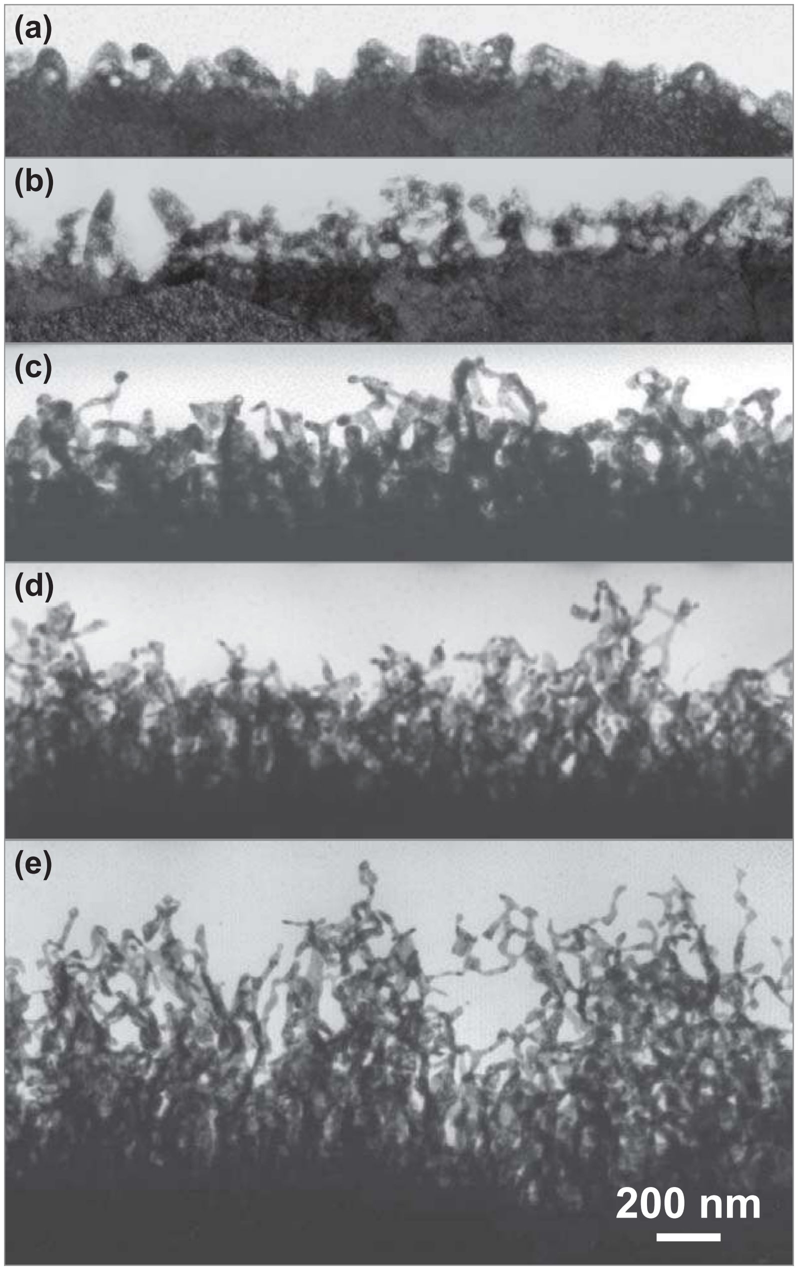
(a)
(b)
(c)
(d)
(e)
200 nm

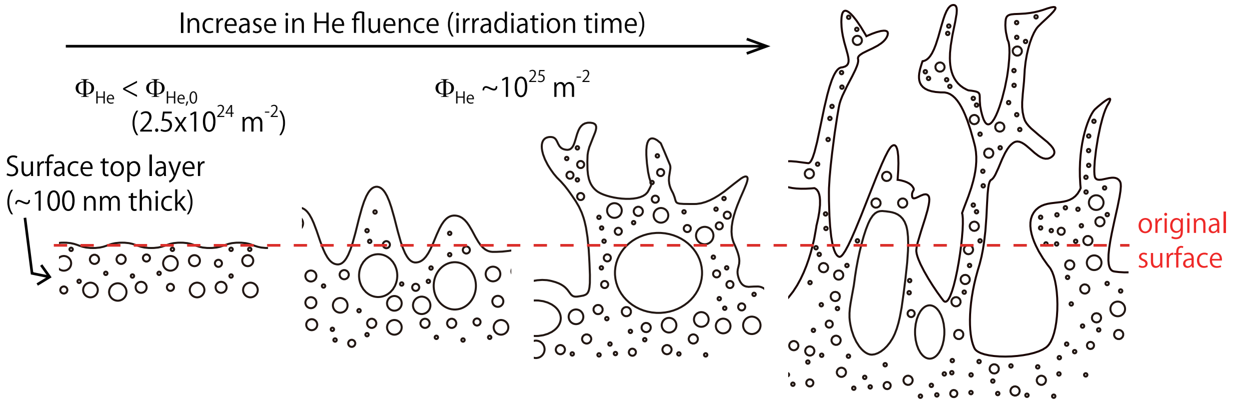
Increase in He fluence (irradiation time)
$\Phi_{He} < \Phi_{He,0}$
$(2.5\times10^{24}\ m^{-2})$
$\Phi_{He} \sim 10^{25}\ m^{-2}$
Surface top layer
(~100 nm thick)
original
surface

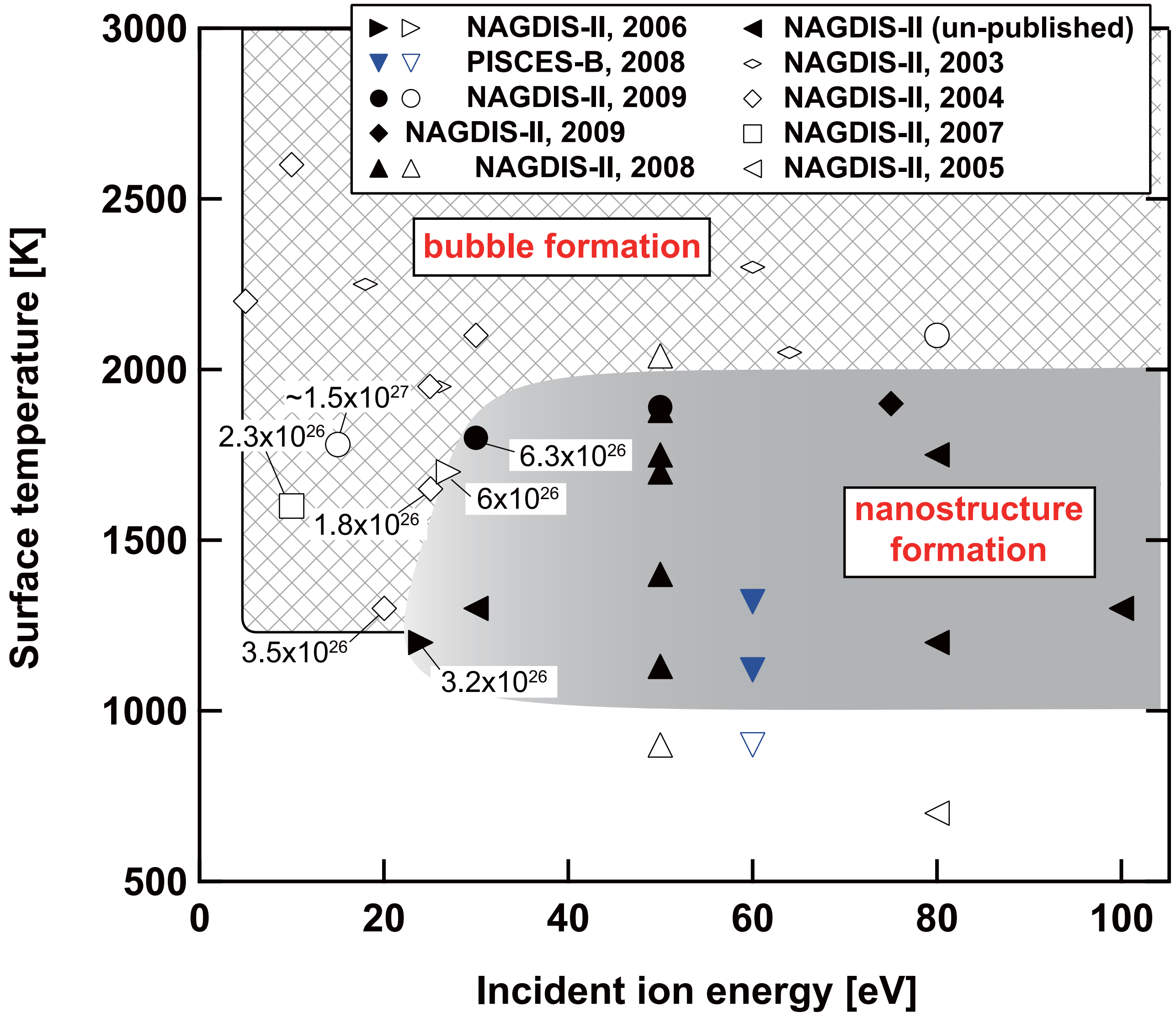
▶ ▷ NAGDIS-II, 2006
▼ ▽ PISCES-B, 2008
● ○ NAGDIS-II, 2009
◆ NAGDIS-II, 2009
▲ △ NAGDIS-II, 2008
◀ NAGDIS-II (un-published)
NAGDIS-II, 2003
◇ NAGDIS-II, 2004
□ NAGDIS-II, 2007
◁ NAGDIS-II, 2005
bubble formation
nanostructure formation
~1.5x10^27
2.3x10^26
6.3x10^26
6x10^26
1.8x10^26
3.5x10^26
3.2x10^26
Surface temperature [K]
3000
2500
2000
1500
1000
500
Incident ion energy [eV]
0
20
40
60
80
100

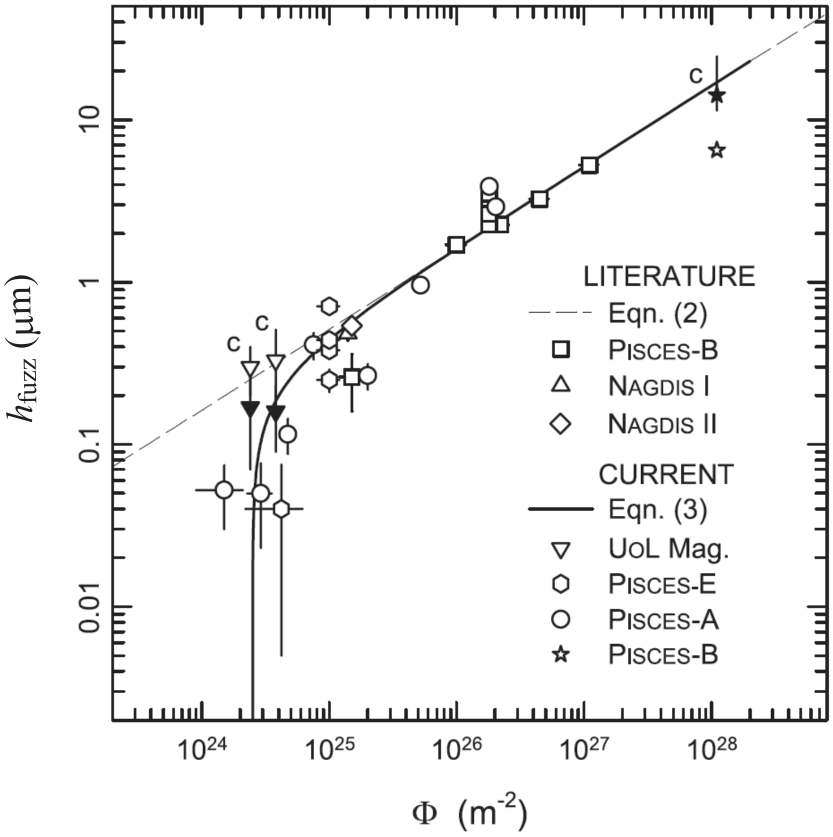
h_{fuzz} (μm)
10
1
0.1
0.01
10^{24}
10^{25}
10^{26}
10^{27}
10^{28}
Φ (m^{-2})
c
c
c
LITERATURE
Eqn. (2)
PISCES-B
NAGDIS I
NAGDIS II
CURRENT
Eqn. (3)
UoL Mag.
PISCES-E
PISCES-A
PISCES-B

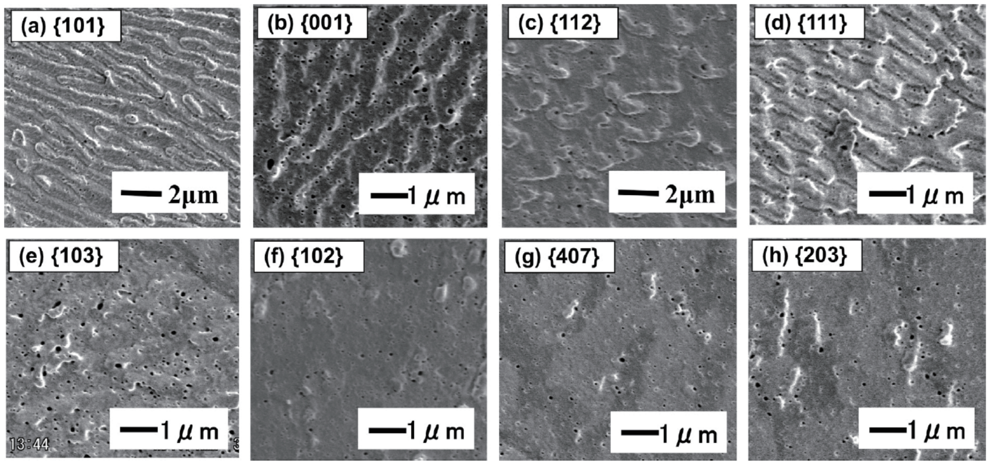
(a) {101}
2μm
(b) {001}
1 μ m
(c) {112}
2μm
(d) {111}
1 μ m
(e) {103}
1 μ m
13:44
(f) {102}
1 μ m
(g) {407}
1 μ m
(h) {203}
1 μ m

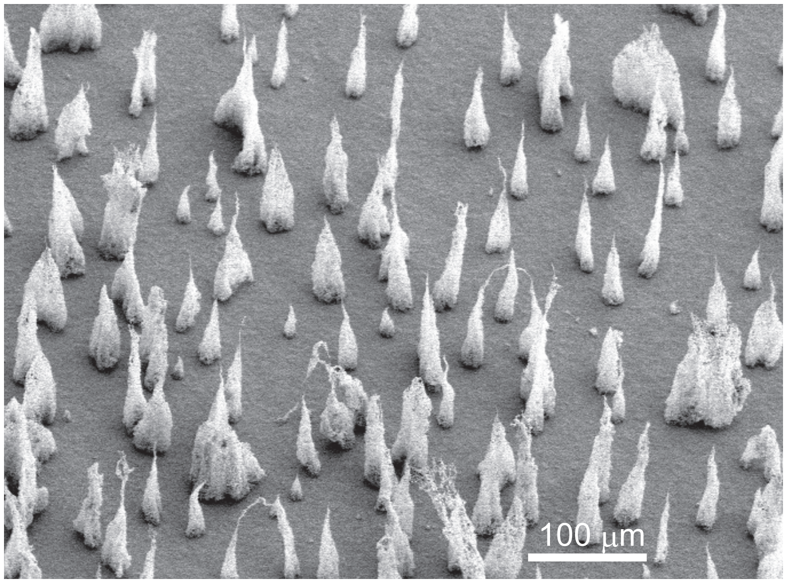
100 µm

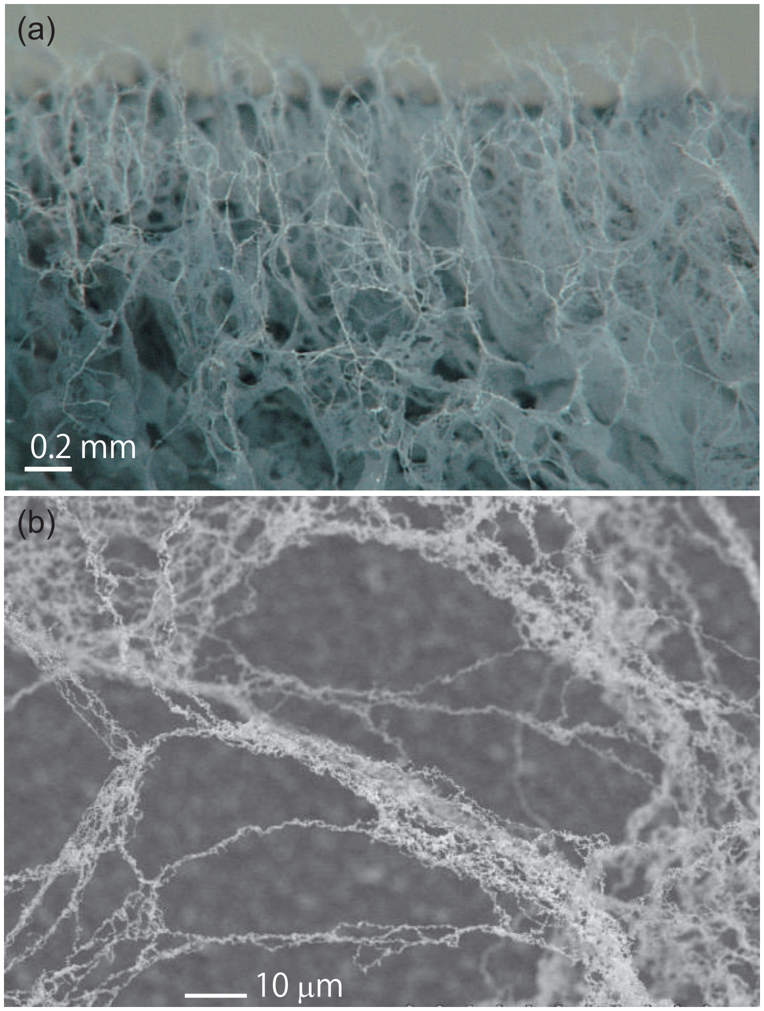
(a)
0.2 mm
(b)
10 μm

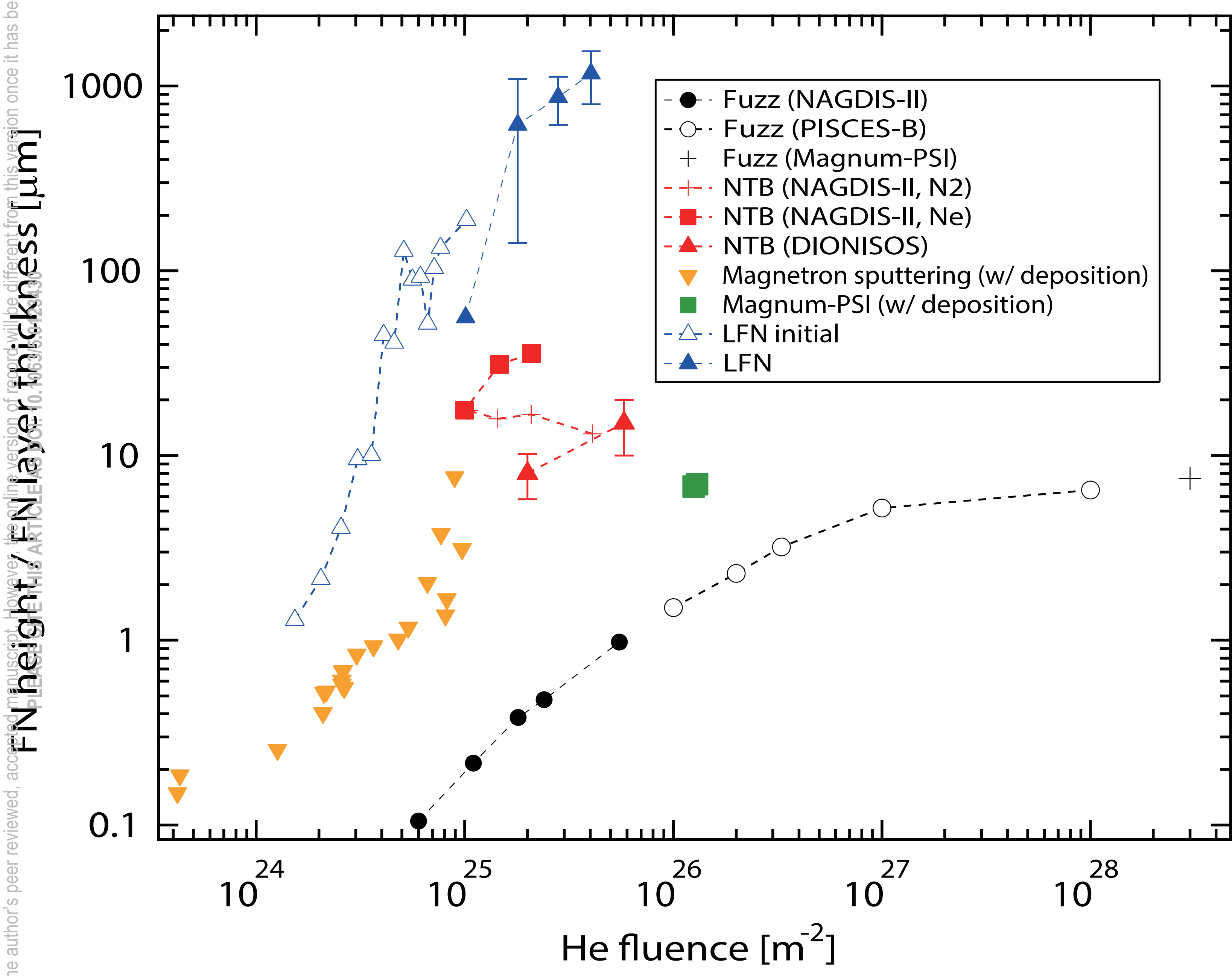
FN height / FN layer thickness [μm]
1000
100
10
1
0.1
10^{24}
10^{25}
10^{26}
10^{27}
10^{28}
He fluence [m^{-2}]
Fuzz (NAGDIS-II)
Fuzz (PISCES-B)
Fuzz (Magnum-PSI)
NTB (NAGDIS-II, N2)
NTB (NAGDIS-II, Ne)
NTB (DIONISOS)
Magnetron sputtering (w/ deposition)
Magnum-PSI (w/ deposition)
LFN initial
LFN

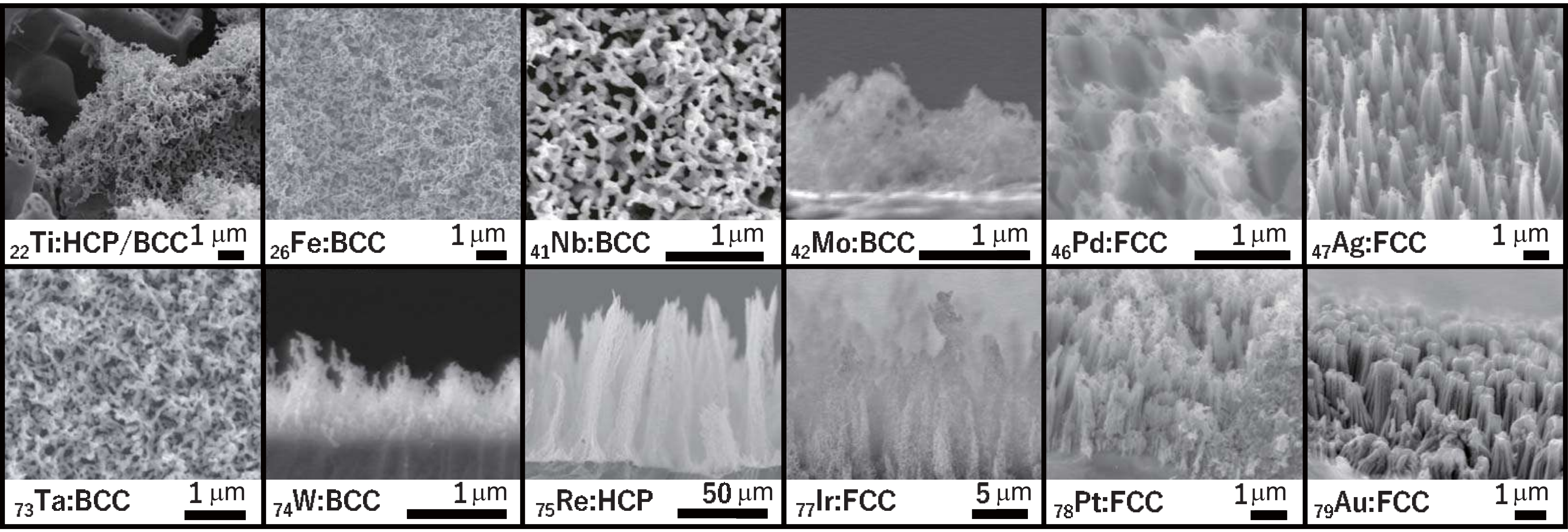
$_{22}$Ti:HCP/BCC
1 μm
$_{26}$Fe:BCC
1 μm
$_{41}$Nb:BCC
1 μm
$_{42}$Mo:BCC
1 μm
$_{46}$Pd:FCC
1 μm
$_{47}$Ag:FCC
1 μm
$_{73}$Ta:BCC
1 μm
$_{74}$W:BCC
1 μm
$_{75}$Re:HCP
50 μm
$_{77}$Ir:FCC
5 μm
$_{78}$Pt:FCC
1 μm
$_{79}$Au:FCC
1 μm

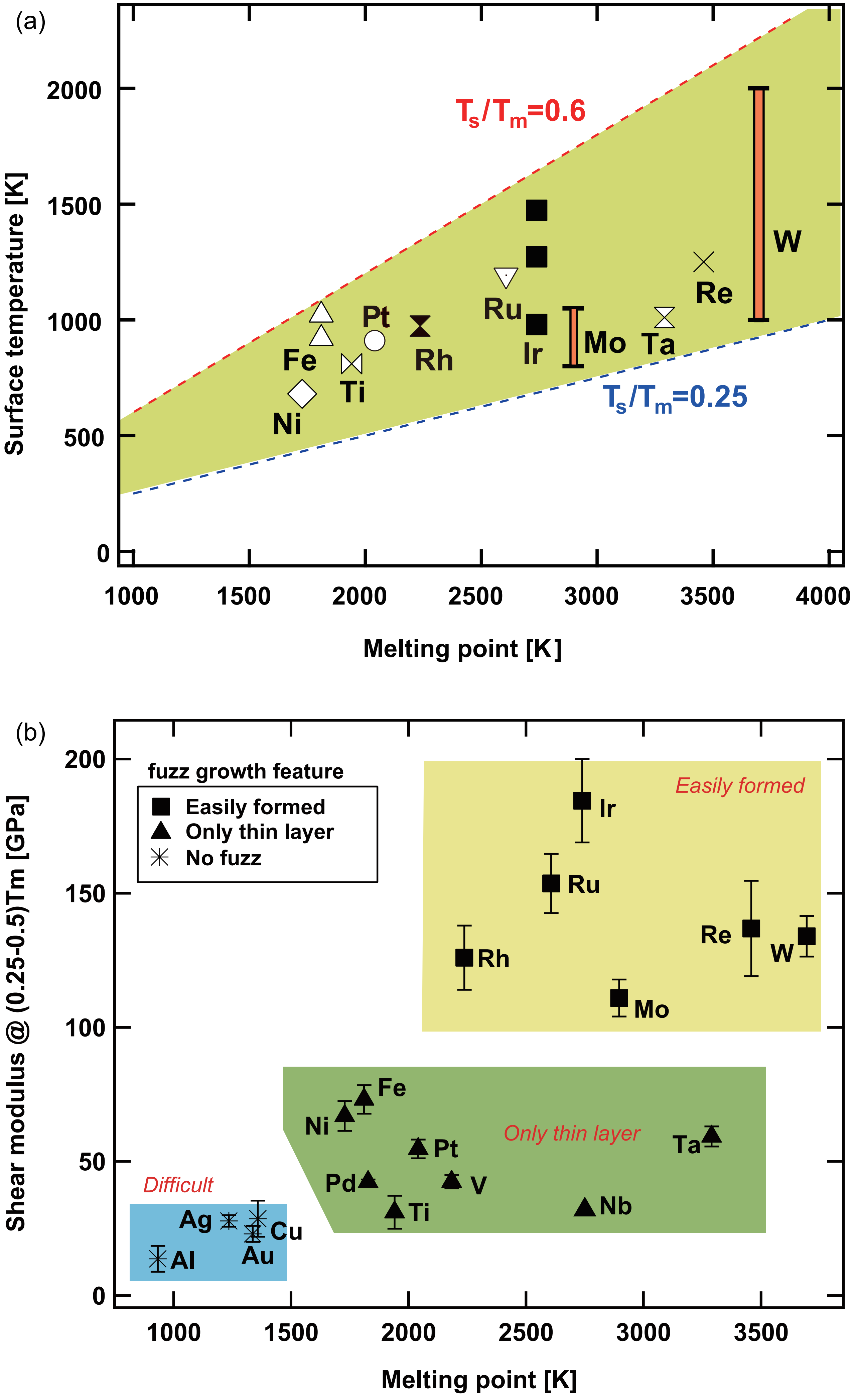
(a)
Surface temperature [K]
0
500
1000
1500
2000
Melting point [K]
1000
1500
2000
2500
3000
3500
4000
T_s/T_m=0.6
T_s/T_m=0.25
Fe
Ni
Ti
Pt
Rh
Ru
Ir
Mo
Ta
Re
W
(b)
Shear modulus @ (0.25-0.5)Tm [GPa]
0
50
100
150
200
Melting point [K]
1000
1500
2000
2500
3000
3500
fuzz growth feature
■ Easily formed
▲ Only thin layer
✳ No fuzz
Easily formed
Only thin layer
Difficult
Ir
Ru
Rh
Re
W
Mo
Fe
Ni
Pt
Pd
V
Ti
Ta
Nb
Ag
Cu
Al
Au

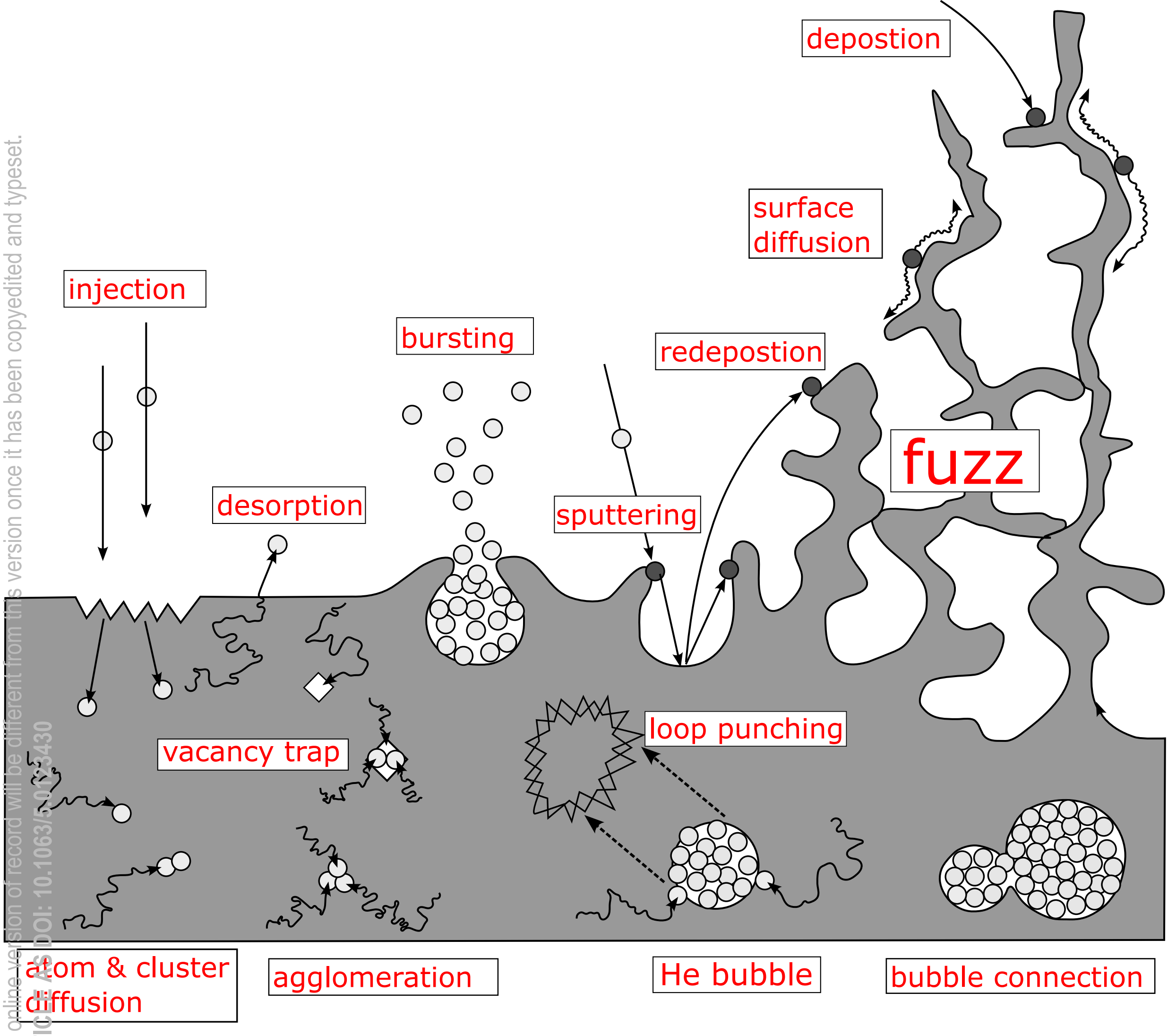
depostion
surface diffusion
injection
bursting
redepostion
desorption
sputtering
fuzz
vacancy trap
loop punching
atom & cluster diffusion
agglomeration
He bubble
bubble connection

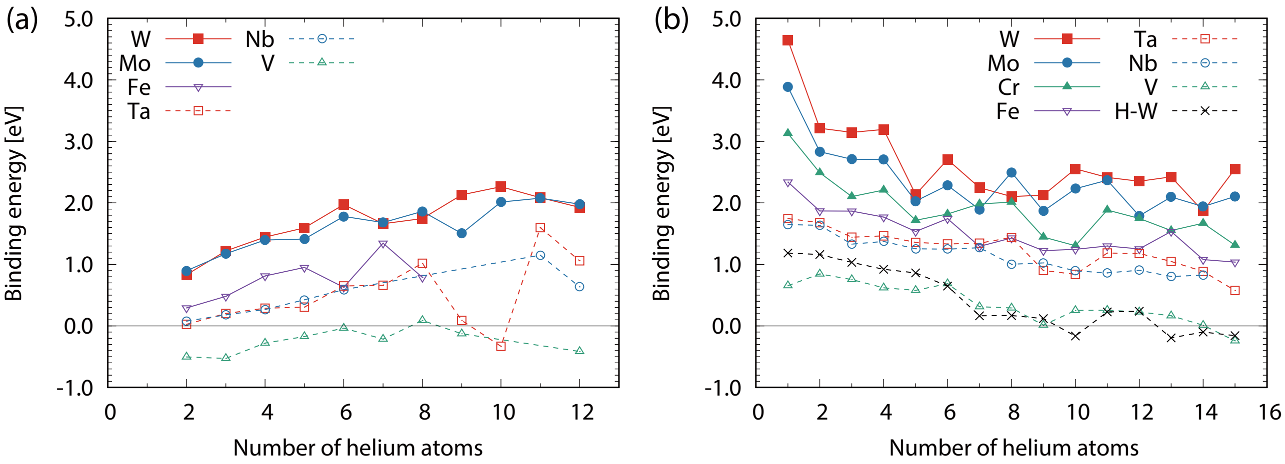
(a)
W
Mo
Fe
Ta
Nb
V
Binding energy [eV]
5.0
4.0
3.0
2.0
1.0
0.0
-1.0
0
2
4
6
8
10
12
Number of helium atoms
(b)
W
Mo
Cr
Fe
Ta
Nb
V
H-W
Binding energy [eV]
5.0
4.0
3.0
2.0
1.0
0.0
-1.0
0
2
4
6
8
10
12
14
16
Number of helium atoms

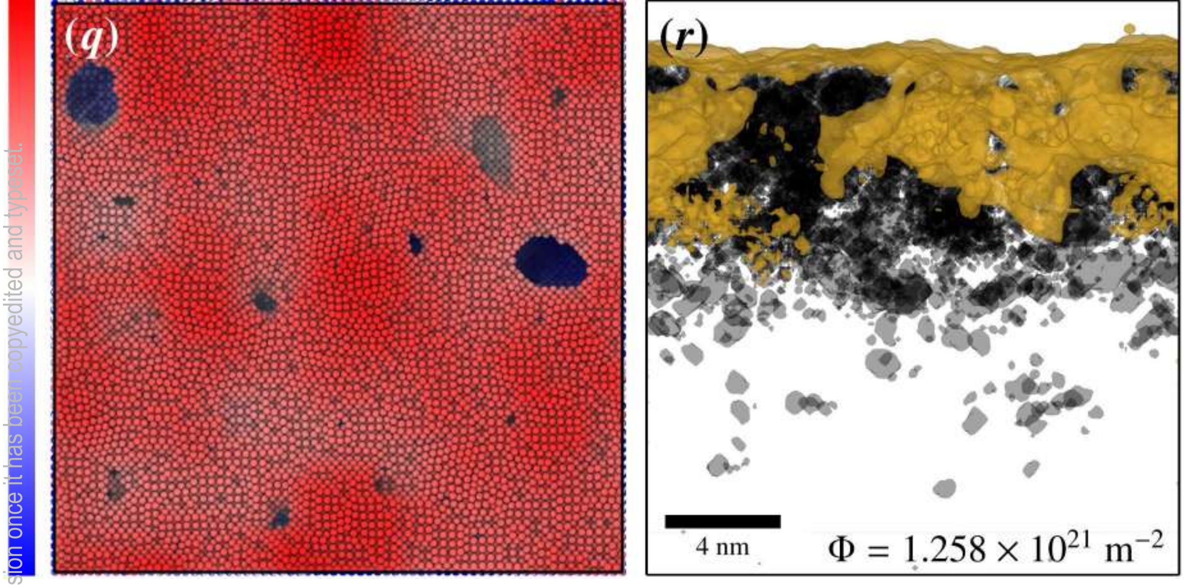
(q)
(r)
4 nm
$\Phi = 1.258 \times 10^{21}\ \mathrm{m}^{-2}$

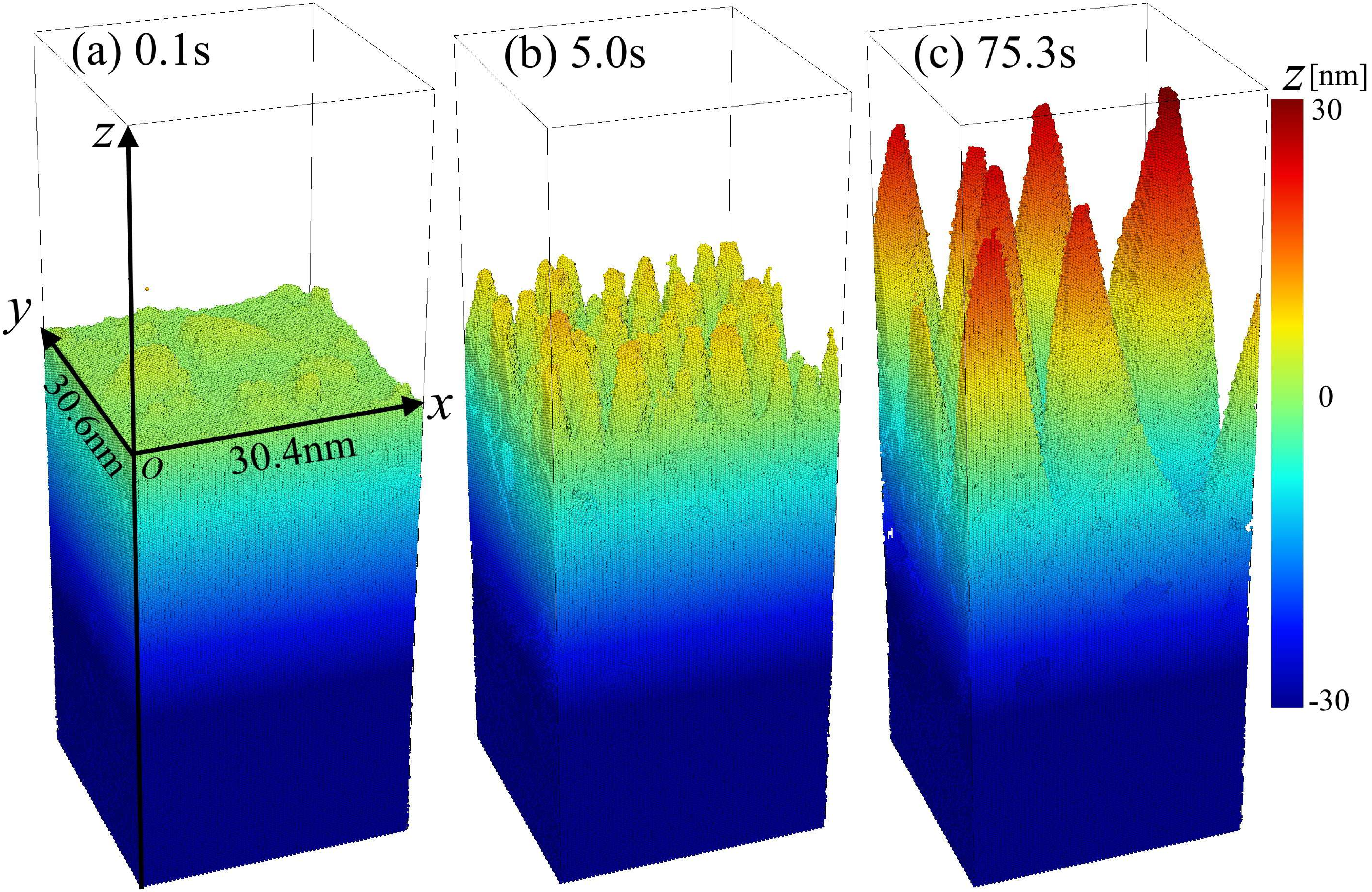
(a) 0.1s
(b) 5.0s
(c) 75.3s
z
y
x
O
30.6nm
30.4nm
z [nm]
30
0
-30

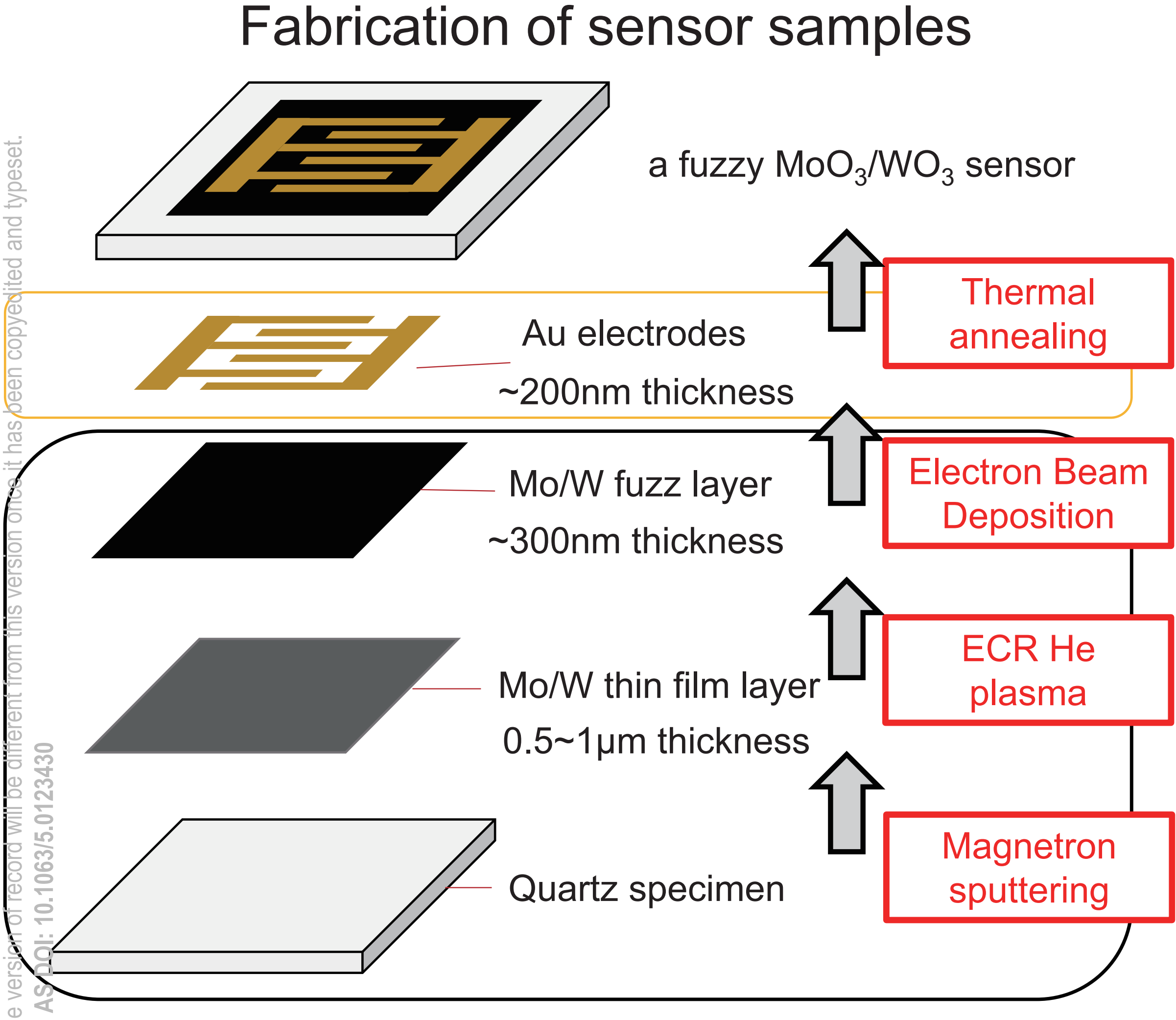
Fabrication of sensor samples
a fuzzy MoO_3/WO_3 sensor
Thermal annealing
Au electrodes
~200nm thickness
Electron Beam Deposition
Mo/W fuzz layer
~300nm thickness
ECR He plasma
Mo/W thin film layer
0.5~1μm thickness
Magnetron sputtering
Quartz specimen

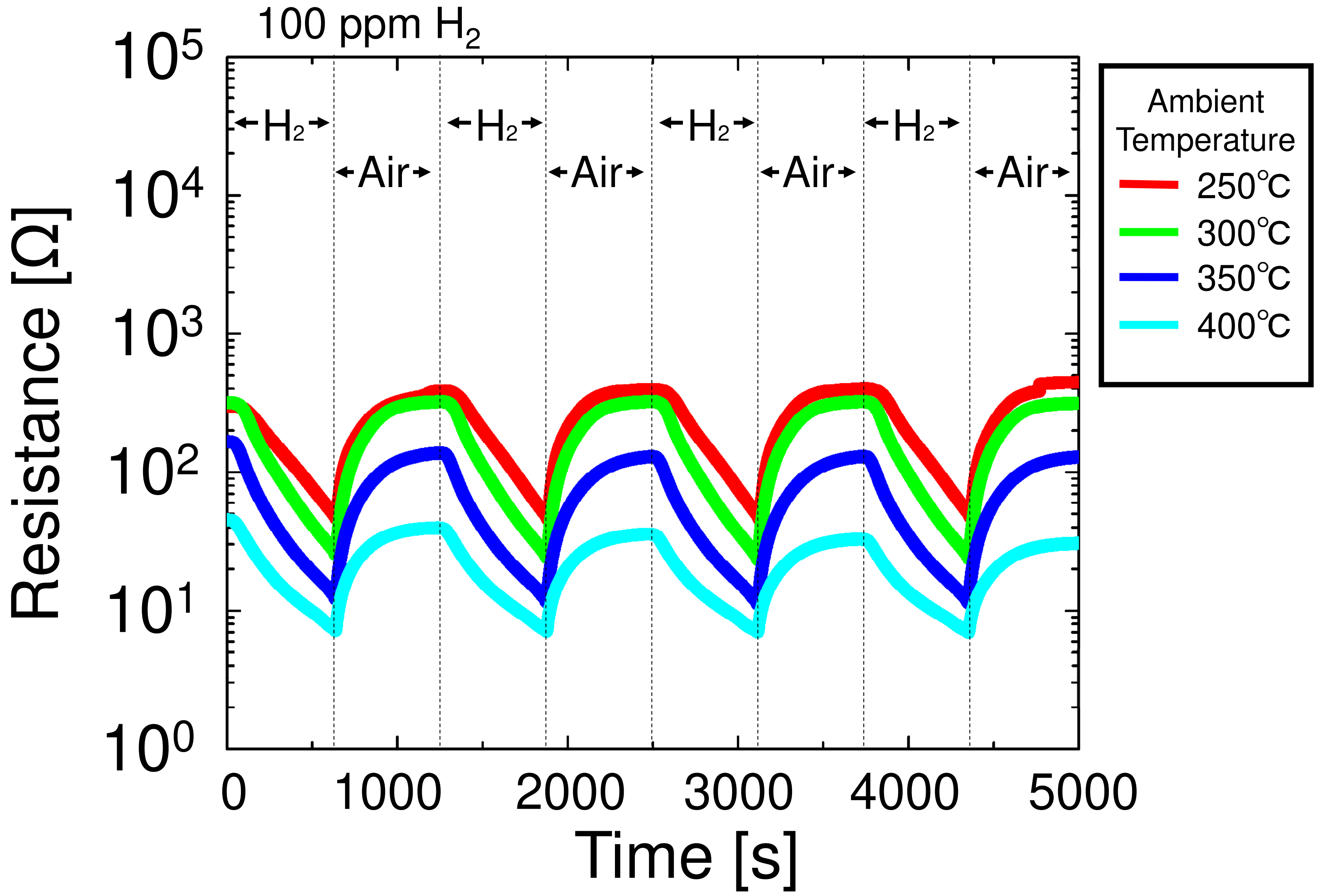
100 ppm H_2
Resistance [Ω]
10^5
10^4
10^3
10^2
10^1
10^0
Time [s]
0
1000
2000
3000
4000
5000
H_2
Air
H_2
Air
H_2
Air
H_2
Air
Ambient Temperature
250°C
300°C
350°C
400°C

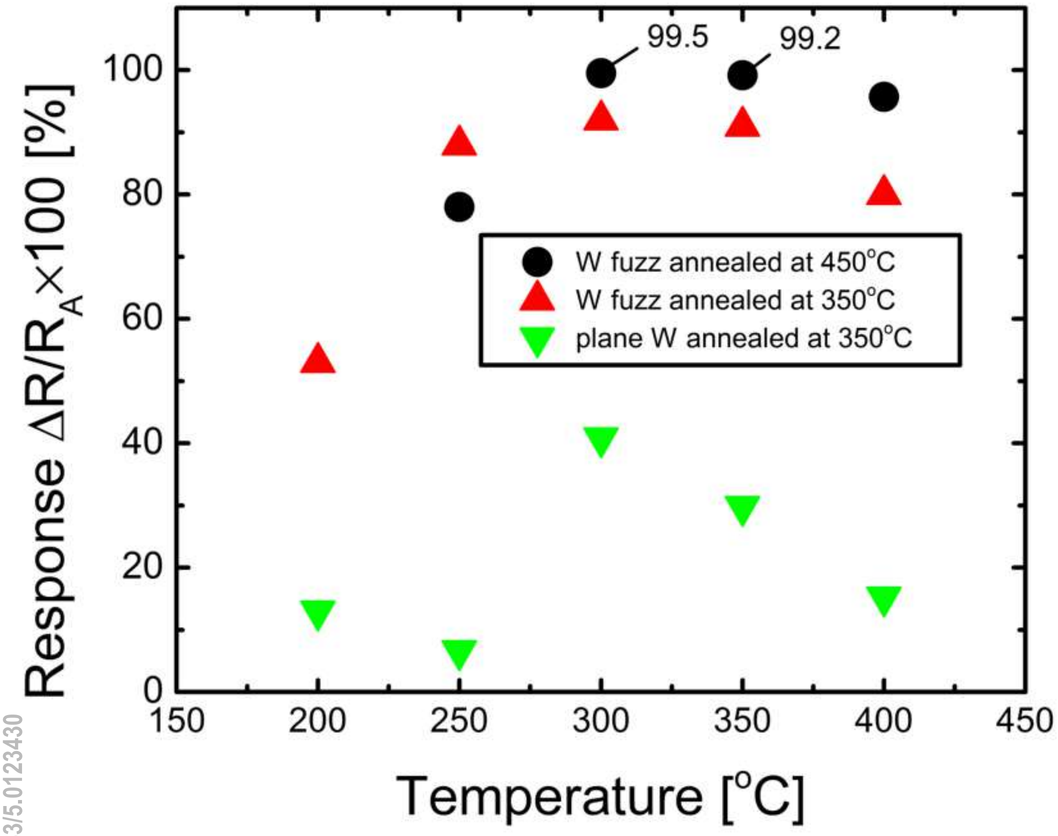
Response $\Delta R/R_A \times 100$ [%]
Temperature [°C]
0
20
40
60
80
100
150
200
250
300
350
400
450
99.5
99.2
● W fuzz annealed at 450°C
▲ W fuzz annealed at 350°C
▼ plane W annealed at 350°C

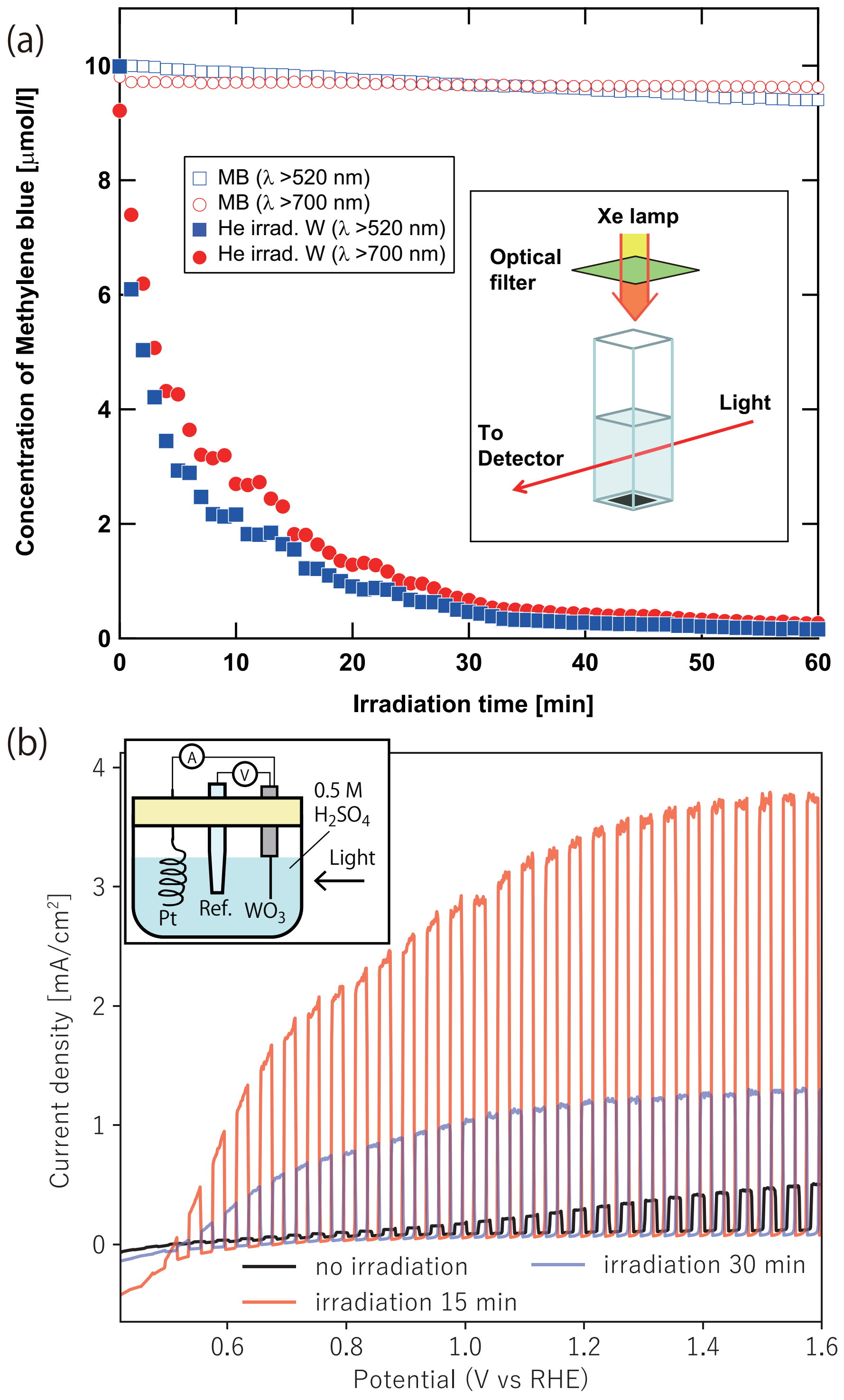
(a)
Concentration of Methylene blue [µmol/l]
0
2
4
6
8
10
0
10
20
30
40
50
60
Irradiation time [min]
□ MB (λ >520 nm)
○ MB (λ >700 nm)
■ He irrad. W (λ >520 nm)
● He irrad. W (λ >700 nm)
Xe lamp
Optical filter
Light
To Detector
(b)
Current density [mA/cm²]
0
1
2
3
4
0.6
0.8
1.0
1.2
1.4
1.6
Potential (V vs RHE)
A
V
0.5 M H₂SO₄
Light
Pt
Ref.
WO₃
no irradiation
irradiation 30 min
irradiation 15 min